Charles University in Prague
Faculty of Mathematics and Physics

Earthquake of Athens, 1999: Study of Aftershocks

Errata to the Master Thesis

Otakar Smrž

Advisor: Doc. RNDr. Jiří Zahradník, DrSc.

Department of Geophysics
Prague, 2001

Errata to Part II

Due to a crucial misunderstanding in station indexing, the results presented in part II of the master thesis are invalid. As the circumstances are pressing, we can only provide the reader with some re-computed data and not embody them in the original work.

The geographical co-ordinates of the stations and the corresponding codes still hold, however their former indices referred to irrelevant seismic records. In Tab. 1, correct assignment is introduced.

In the thesis, the choice of inversion sets was based on the quality of the records. That is why we keep to station indices in our re-computations, even though the implied spatial distribution may not be optimal. Poor-polarity check-points are obtained by way of intersection.

Hoping to fit the plateau of the transfer function more reliably, we reset the lower limit of the inversion frequency domain $\mathcal{F}$, which now features

$$f_{min} = 1.5 \text{ Hz} \qquad f_{max} = 2.0 \text{ Hz} \qquad \Delta f = 50/4096 \text{ Hz}.$$

The new results are not interpreted separately since the method explained in the thesis is fully applicable. Special attention should be paid to the extra chapter E and to the reviewed conclusion.

Id	Code	North Latitude		East Longitude		Altitude
1	MAG	38° 04.37′	38.073°	23° 32.00′	23.533°	35 m
2	INF	38° 18.31′	38.305°	23° 38.67′	23.645°	36 m
3	ORP	38° 18.97′	38.316°	23° 47.32′	23.789°	148 m
4	MAR	38° 09.45′	38.157°	23° 57.44′	23.957°	46 m
5	SPT	37° 57.92′	37.965°	23° 54.73′	23.912°	178 m
6	VUL	37° 48.42′	37.807°	23° 47.09′	23.785°	29 m
7	RAF	38° 01.08′	38.018°	23° 59.69′	23.995°	78 m
8	VAR	38° 13.37′	38.223°	23° 54.97′	23.916°	450 m
9	KAL	38° 15.72′	38.262°	23° 52.39′	23.873°	596 m
10	HAI	38° 00.77′	38.013°	23° 38.22′	23.637°	200 m
11	MEL	38° 03.67′	38.061°	23° 50.87′	23.848°	350 m
12	THR	38° 08.37′	38.139°	23° 45.63′	23.761°	451 m
13	MEN	38° 05.63′	38.094°	23° 43.43′	23.724°	110 m
14	FIL	38° 06.24′	38.104°	23° 40.18′	23.670°	437 m
15	MKL	38° 07.82′	38.130°	23° 39.39′	23.657°	484 m
16	PAR	38° 09.15′	38.153°	23° 44.20′	23.737°	1109 m
17	KRY	38° 08.45′	38.141°	23° 49.70′	23.828°	559 m
18	TAT	38° 09.40′	38.157°	23° 47.79′	23.797°	523 m
19	FLP	37° 58.19′	37.970°	23° 43.21′	23.720°	140 m
20	BAR	38° 08.08′	38.135°	23° 47.45′	23.791°	435 m
21	ASP	38° 03.72′	38.062°	23° 35.33′	23.589°	35 m
22	STE	38° 10.46′	38.174°	23° 32.77′	23.546°	631 m
23	AHA	38° 04.99′	38.083°	23° 45.91′	23.765°	225 m
24	HAL	38° 01.33′	38.022°	23° 47.87′	23.798°	31 m
25	KIF	38° 05.76′	38.096°	23° 47.97′	23.799°	36 m
26	FLD	38° 02.45′	38.041°	23° 44.01′	23.733°	25 m
27	LIO	38° 04.60′	38.077°	23° 42.53′	23.709°	182 m
28	SAL	37° 59.05′	37.984°	23° 28.77′	23.480°	71 m
29	NLI	38° 02.29′	38.038°	23° 42.07′	23.701°	36 m
20	PET	38° 02.76′	38.046°	23° 39.95′	23.666°	312 m
31	GEO	37° 58.92′	37.982°	23° 42.14′	23.702°	60 m

Table 1: List of available stations and their co-ordinates.

Chapter A

Aftershock 2671010

This inversion engages just nine stations because there have been persistent doubts of the data from station 31. The reduction shows up in absolute values of all error functions based on the improved normalization, whereas the former normalization involves re-scaling by the number of stations (see the appropriate definitions).

A.0.1 Computation A/9

For error functions and depth plots, see Figs. A.2, A.3. No consistent solution can be found.

A.0.2 Computation X/9

For error functions and depth plots, see Figs. A.5, A.4. No consistent solution can be found.

Id	Code	Lat N (deg)	Lon E (deg)	Azimuth (deg)	Distance (km)
2	INF	38.305	23.645	12.63	26.30
5	SPT	37.965	23.912	112.47	31.56
9	KAL	38.262	23.873	50.79	33.10
11	MEL	38.061	23.848	93.44	23.57
13	MEN	38.094	23.724	80.03	12.87
16	PAR	38.153	23.737	57.52	16.36
22	STE	38.174	23.546	345.45	11.48
23	AHA	38.083	23.765	86.43	16.30
26	FLD	38.041	23.733	105.19	13.96

Table A.1: Stations engaged in the inversion (2671010 AX).

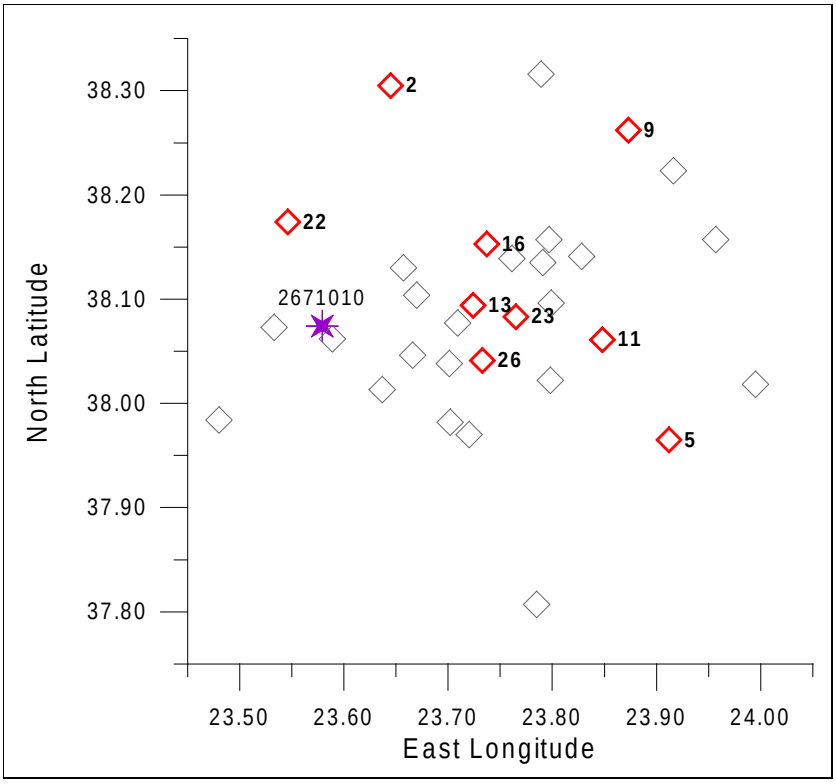

Figure A.1: Aftershock epicentre & deployment of the stations (2671010 AX).

Code	Azim (deg)	Take-off Angles (deg)								Sign
INF	12	97	104	109	113	108	115	120	124	U
SPT	112	95	101	105	109	102	109	114	118	D
KAL	50	95	100	104	108	100	107	112	116	U
MEL	93	99	106	111	116	113	119	123	127	D
MEN	80	113	122	129	134	135	139	143	146	D
PAR	57	106	115	121	127	126	131	135	139	U
STE	345	117	126	132	138	138	143	146	149	U
AHA	86	107	115	122	127	126	131	136	139	D
FLD	105	111	120	126	132	132	137	140	144	D
MAG	268	149	155	159	162	163	165	167	168	D
ORP	34	95	100	105	109	100	108	113	117	U
MAR	74	95	99	104	107	99	106	111	115	U
VUL	148	95	99	103	107	98	106	111	115	U
RAF	99	94	98	102	106	97	104	109	113	D
VAR	60	95	100	104	108	99	107	112	116	U
HAI	143	127	135	142	146	147	151	154	156	D
KRY	71	99	106	112	117	113	120	124	128	U
HAL	106	102	110	116	121	119	124	129	133	D
KIF	82	102	110	117	122	120	125	130	134	U
LIO	88	117	126	133	138	139	143	146	149	D

Table A.2: Stations providing polarity data & take-off angles of the first--arrival rays (depth increasing to the right, see depth plots) (2671010 AX).

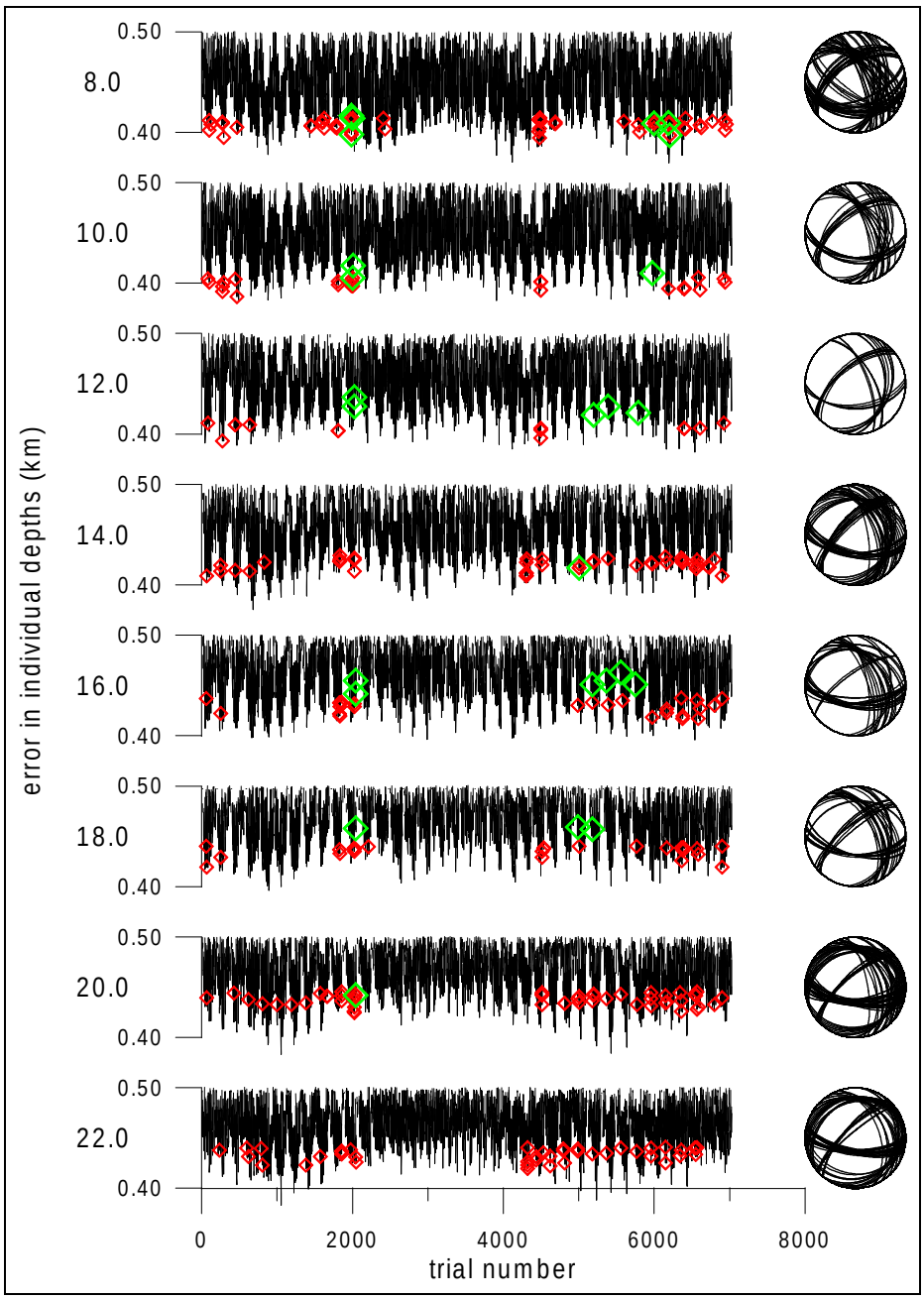

Figure A.2: Depth plot of E (black), poor-polarity P (red) and rich-polarity P (green), along with poor-polarity beach balls (2671010 A/9).

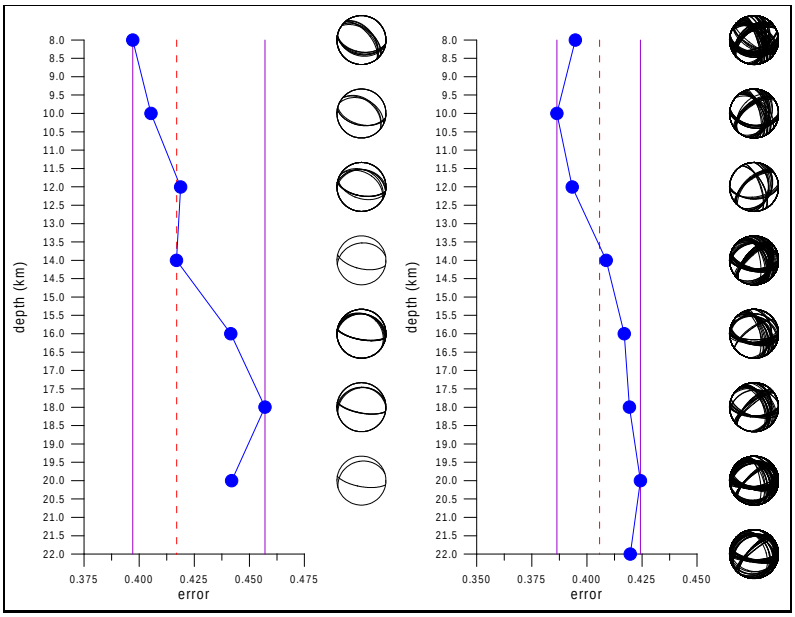

Figure A.3: Depth plot of $P(\phi_P, \delta_P, \lambda_P)$ & beach balls (2671010 A/20, A/9).

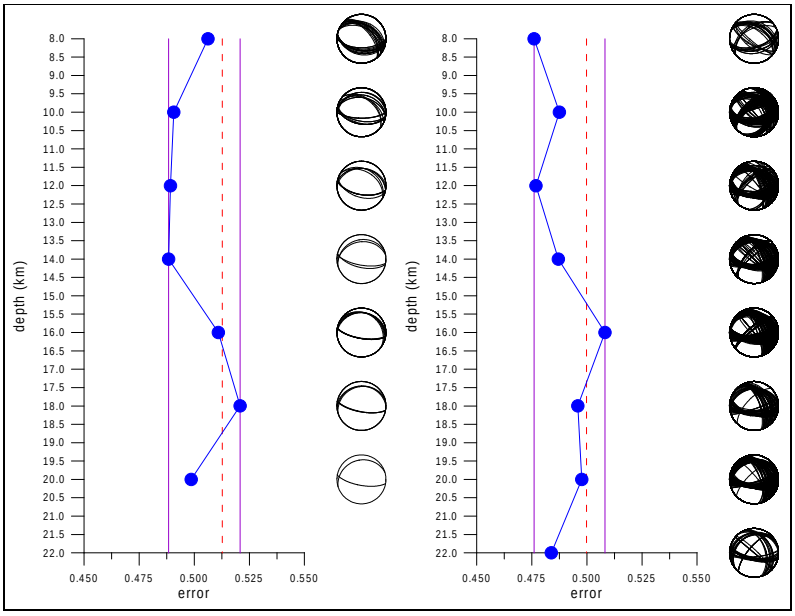

Figure A.4: Depth plot of $P(\phi_P, \delta_P, \lambda_P)$ & beach balls (2671010 X/20, X/9).

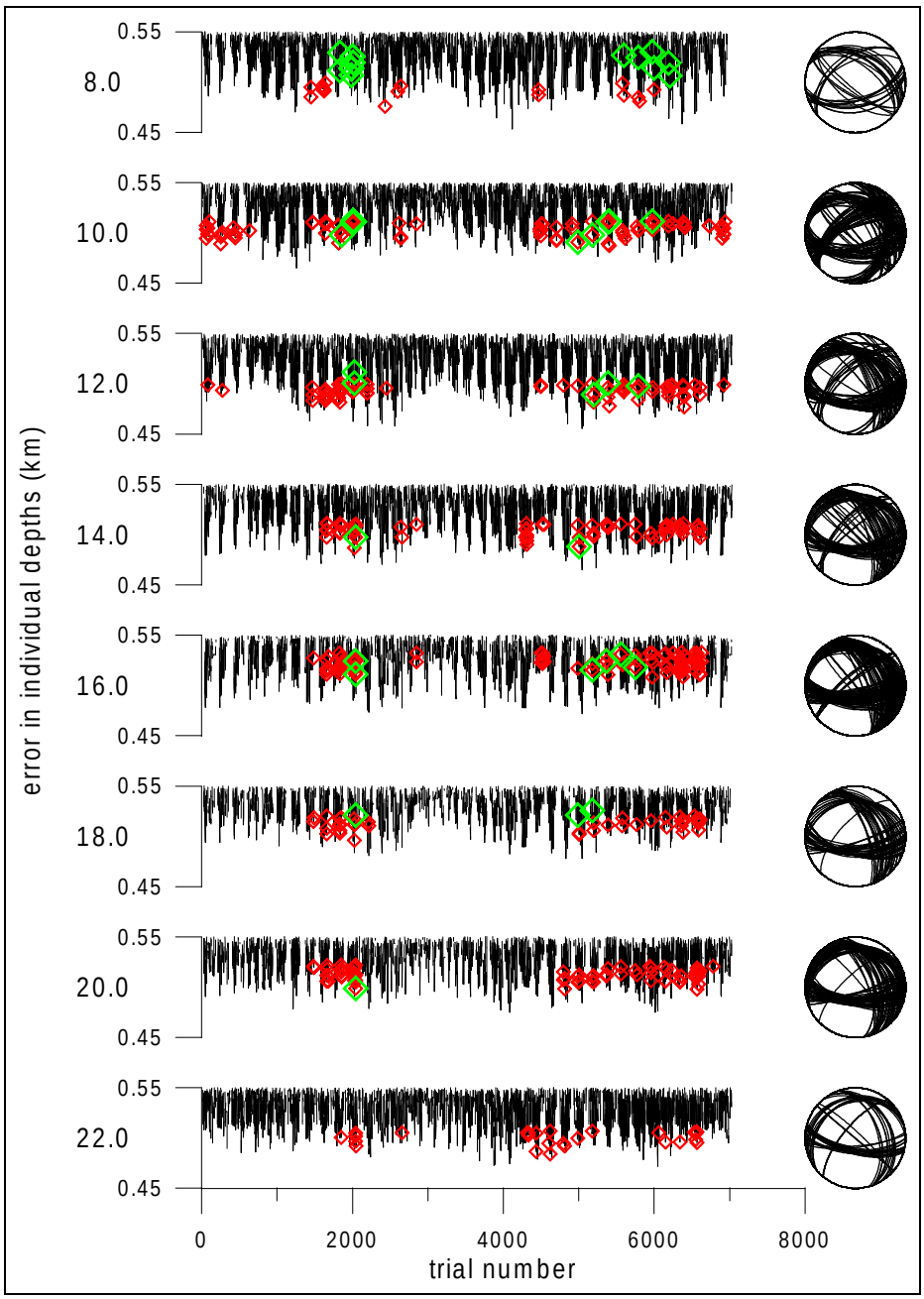

Figure A.5: Depth plot of E (black), poor-polarity P (red) and rich-polarity P (green), along with poor-polarity beach balls (2671010 X/9).

Chapter B

Aftershock 2761700

B.1 First station set

Nine stations were used for this inversion, station 31 was ignored.

B.1.1 Computation A/9

No consistent solution can be found, see Figs. B.2, B.3.

B.1.2 Computation X/9

No consistent solution can be found, see Figs. B.5, B.4.

B.2 Second station set

Nine stations were used, station 1 was ignored this time.

B.2.1 Computation B/9

No consistent solution can be found, see Figs. B.7, B.8.

B.2.2 Computation Y/9

No consistent solution can be found, see Figs. B.10, B.9.

Id	Code	Lat N (deg)	Lon E (deg)	Azimuth (deg)	Distance (km)
5	SPT	37.965	23.912	137.35	19.78
11	MEL	38.061	23.848	116.54	8.70
13	MEN	38.094	23.724	265.82	3.07
15	MKL	38.130	23.657	292.97	9.68
20	BAR	38.135	23.791	32.84	5.15
22	STE	38.174	23.546	295.02	20.53
23	AHA	38.083	23.765	160.13	1.54
26	FLD	38.041	23.733	200.43	6.52
27	LIO	38.077	23.709	244.23	4.86

Table B.1: Stations engaged in the inversion (2761700 AX).

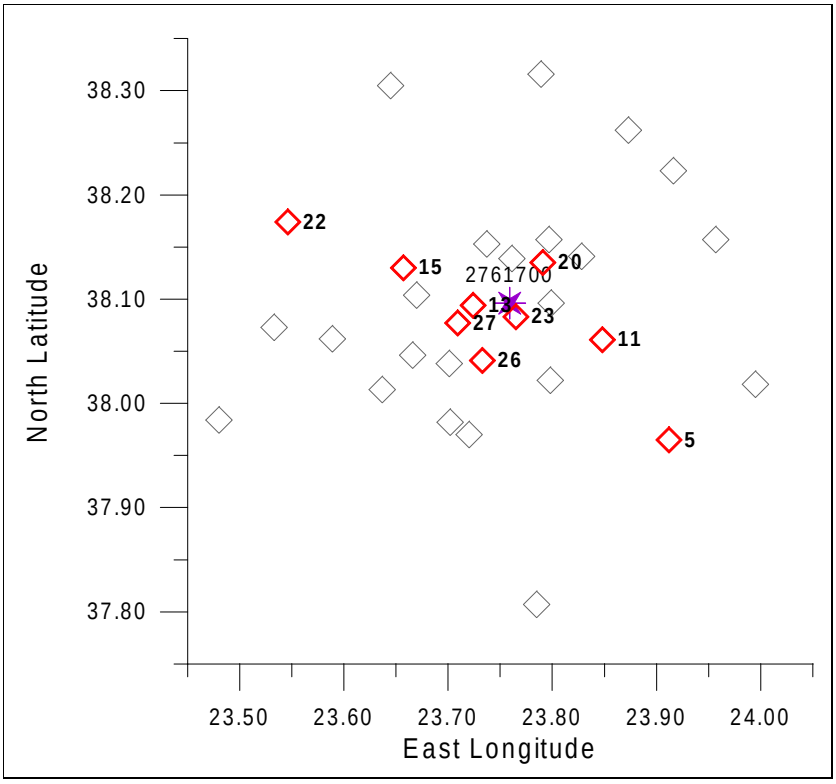

Figure B.1: Aftershock epicentre & deployment of the stations (2761700 AX).

Code	Azim (deg)	Take-off Angles (deg)								Sign
SPT	137	103	93	99	104	108	112	115	117	D
MEL	116	119	116	123	128	133	136	139	142	D
MEN	265	148	150	154	157	160	162	163	165	D
MKL	292	116	112	120	125	129	133	136	139	D
BAR	32	133	135	140	145	148	151	153	155	U
STE	295	102	93	99	103	107	111	114	116	D
AHA	160	163	164	166	168	169	170	171	172	U
FLD	200	127	127	133	138	141	145	147	150	U
LIO	244	135	137	142	146	150	152	155	157	U
ORP	6	100	92	96	100	103	106	109	112	U
MAR	68	104	94	101	106	110	113	116	119	U
VUL	175	98	91	94	96	99	101	104	106	U
RAF	112	101	92	97	102	105	109	111	114	D
VAR	44	103	93	100	104	108	112	115	118	U
KAL	28	102	93	98	103	107	110	113	116	U
HAI	229	108	99	108	113	117	121	124	127	U
THR	2	136	137	143	147	150	153	155	157	D
PAR	343	126	126	132	137	141	144	147	150	D
KRY	50	121	120	127	132	136	139	142	145	U
HAL	157	118	115	122	128	132	135	139	141	U
KIF	90	145	147	151	155	157	159	161	163	U
GEO	201	109	100	109	114	118	122	125	128	U

Table B.2: Stations providing polarity data & take-off angles of the first--arrival rays (depth increasing to the right, see depth plots) (2761700 AX).

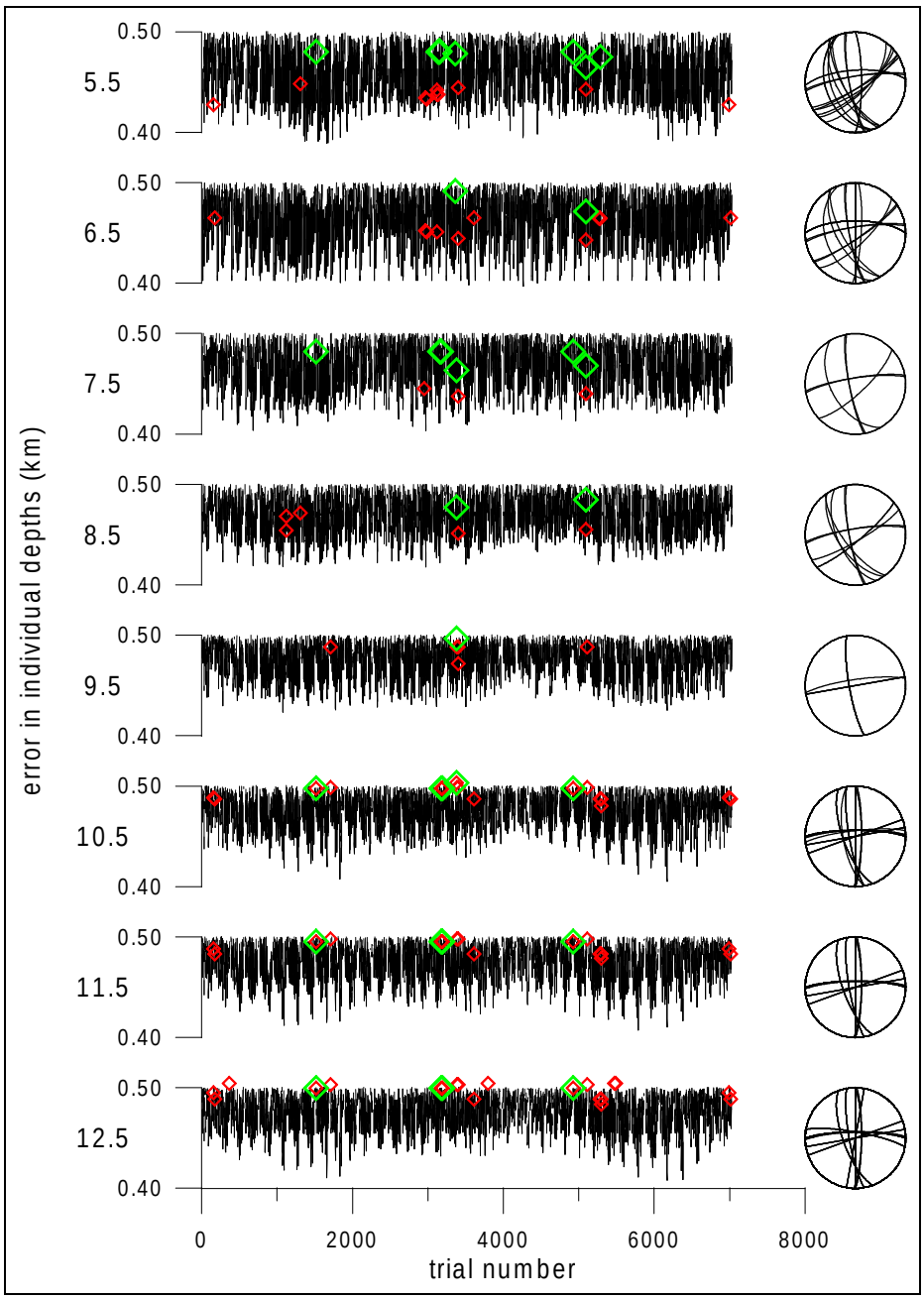

Figure B.2: Depth plot of E (black), poor-polarity P (red) and rich-polarity P (green), along with poor-polarity beach balls (2761700 A/9).

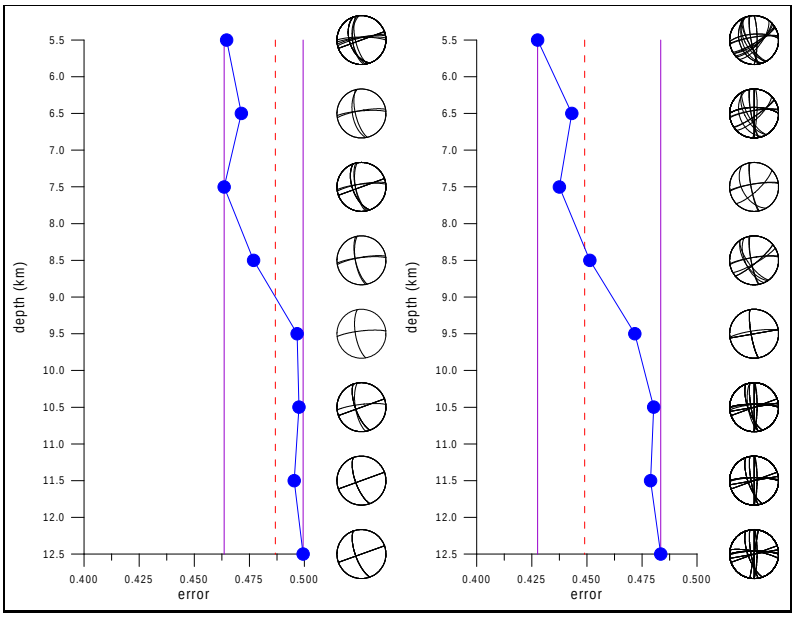

Figure B.3: Depth plot of $P(\phi_P, \delta_P, \lambda_P)$ & beach balls (2761700 A/22, A/9).

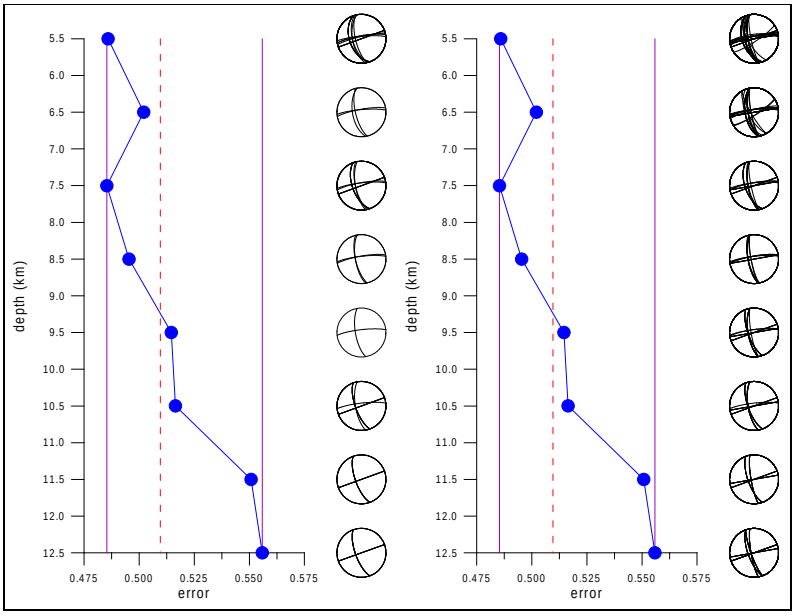

Figure B.4: Depth plot of $P(\phi_P, \delta_P, \lambda_P)$ & beach balls (2761700 X/22, X/9).

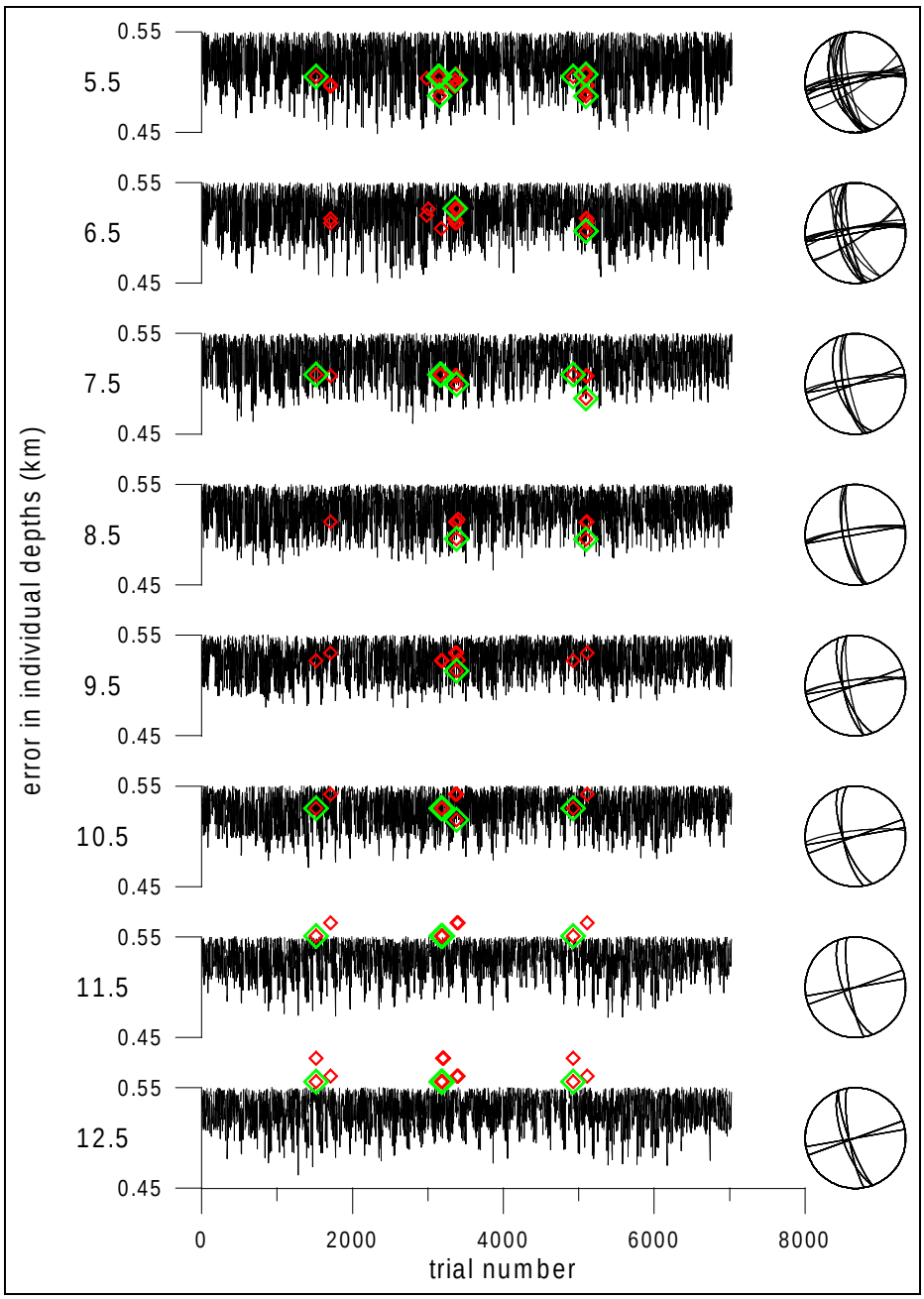

Figure B.5: Depth plot of E (black), poor-polarity P (red) and rich-polarity P (green), along with poor-polarity beach balls (2761700 X/9).

Id	Code	Lat N (deg)	Lon E (deg)	Azimuth (deg)	Distance (km)
3	ORP	38.316	23.789	6.10	24.58
4	MAR	38.157	23.957	68.56	18.58
6	VUL	37.807	23.785	175.94	32.19
7	RAF	38.018	23.995	112.70	22.39
9	KAL	38.262	23.873	28.33	20.96
12	THR	38.139	23.761	2.08	4.78
16	PAR	38.153	23.737	343.10	6.62
17	KRY	38.141	23.828	50.33	7.83
25	KIF	38.096	23.799	90.03	3.50

Table B.3: Stations engaged in the inversion (2761700 BY).

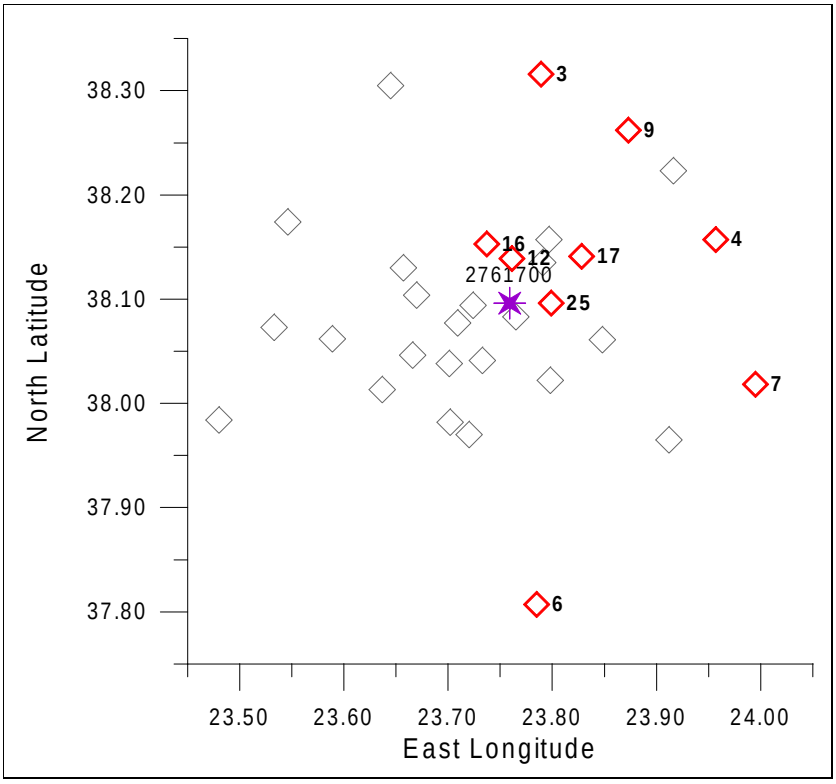

Figure B.6: Aftershock epicentre & deployment of the stations (2761700 BY).

Code	Azim (deg)	Take-off Angles (deg)								Sign
ORP	6	100	92	96	100	103	106	109	112	U
MAR	68	104	94	101	106	110	113	116	119	U
VUL	175	98	91	94	96	99	101	104	106	U
RAF	112	101	92	97	102	105	109	111	114	D
KAL	28	102	93	98	103	107	110	113	116	U
THR	2	136	137	143	147	150	153	155	157	D
PAR	343	126	126	132	137	141	144	147	150	D
KRY	50	121	120	127	132	136	139	142	145	U
KIF	90	145	147	151	155	157	159	161	163	U
SPT	137	103	93	99	104	108	112	115	117	D
VAR	44	103	93	100	104	108	112	115	118	U
HAI	229	108	99	108	113	117	121	124	127	U
MEL	116	119	116	123	128	133	136	139	142	D
MEN	265	148	150	154	157	160	162	163	165	D
MKL	292	116	112	120	125	129	133	136	139	D
BAR	32	133	135	140	145	148	151	153	155	U
STE	295	102	93	99	103	107	111	114	116	D
AHA	160	163	164	166	168	169	170	171	172	U
HAL	157	118	115	122	128	132	135	139	141	U
FLD	200	127	127	133	138	141	145	147	150	U
LIO	244	135	137	142	146	150	152	155	157	U
GEO	201	109	100	109	114	118	122	125	128	U

Table B.4: Stations providing polarity data & take-off angles of the first--arrival rays (depth increasing to the right, see depth plots) (2761700 BY).

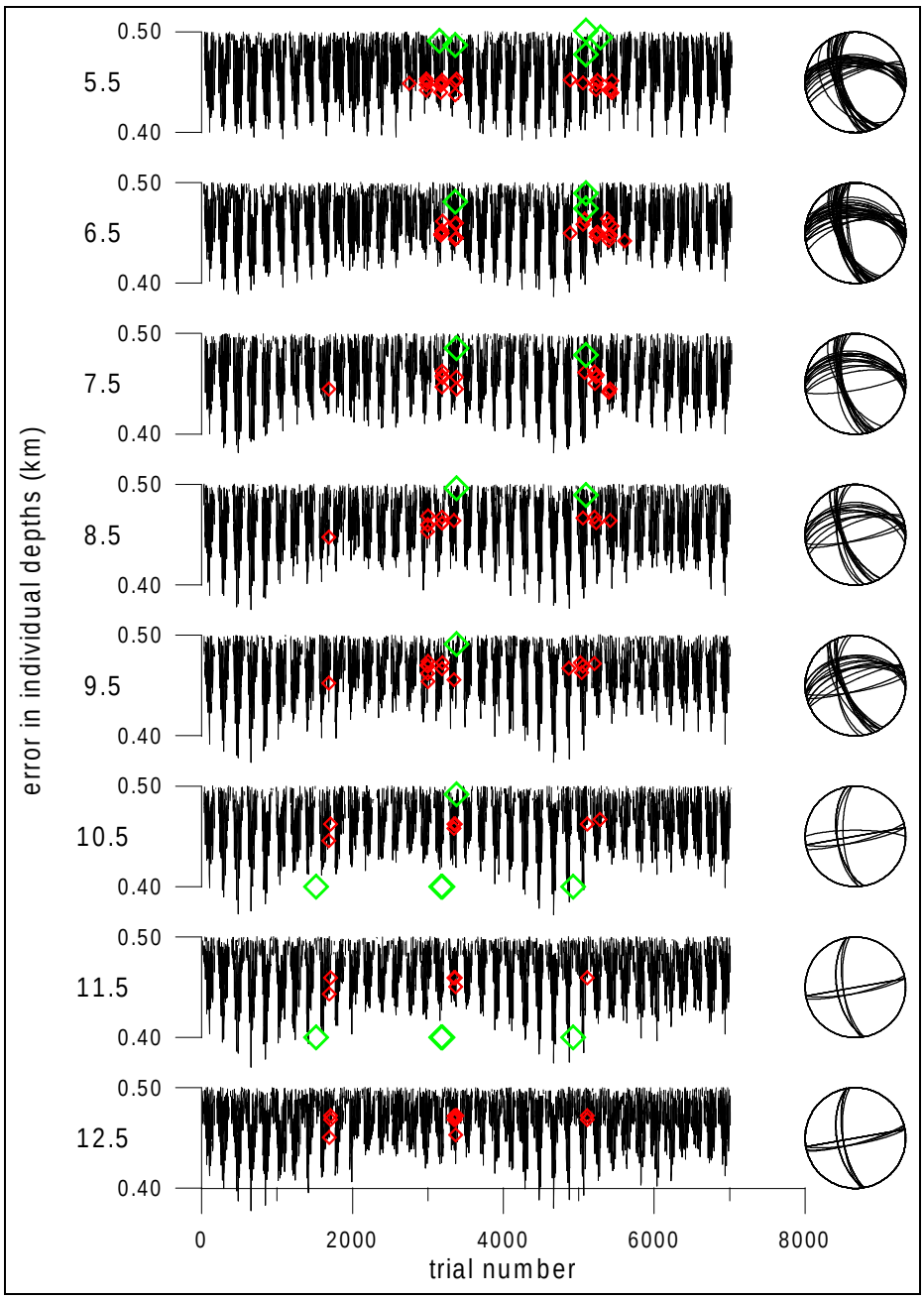

Figure B.7: Depth plot of E (black), poor-polarity P (red) and rich-polarity P (green), along with poor-polarity beach balls (2761700 B/9).

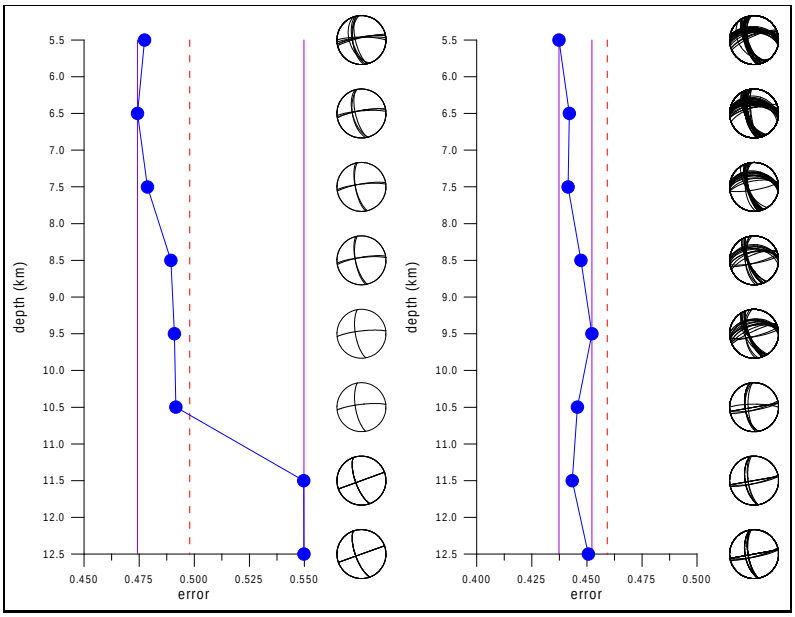

Figure B.8: Depth plot of $P(\phi_P, \delta_P, \lambda_P)$ & beach balls (2761700 B/22, B/9).

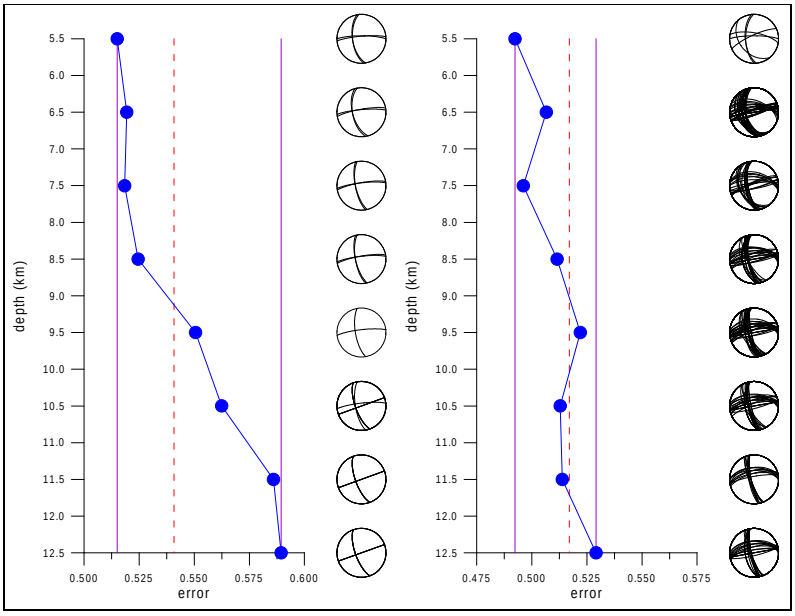

Figure B.9: Depth plot of $P(\phi_P, \delta_P, \lambda_P)$ & beach balls (2761700 Y/22, Y/9).

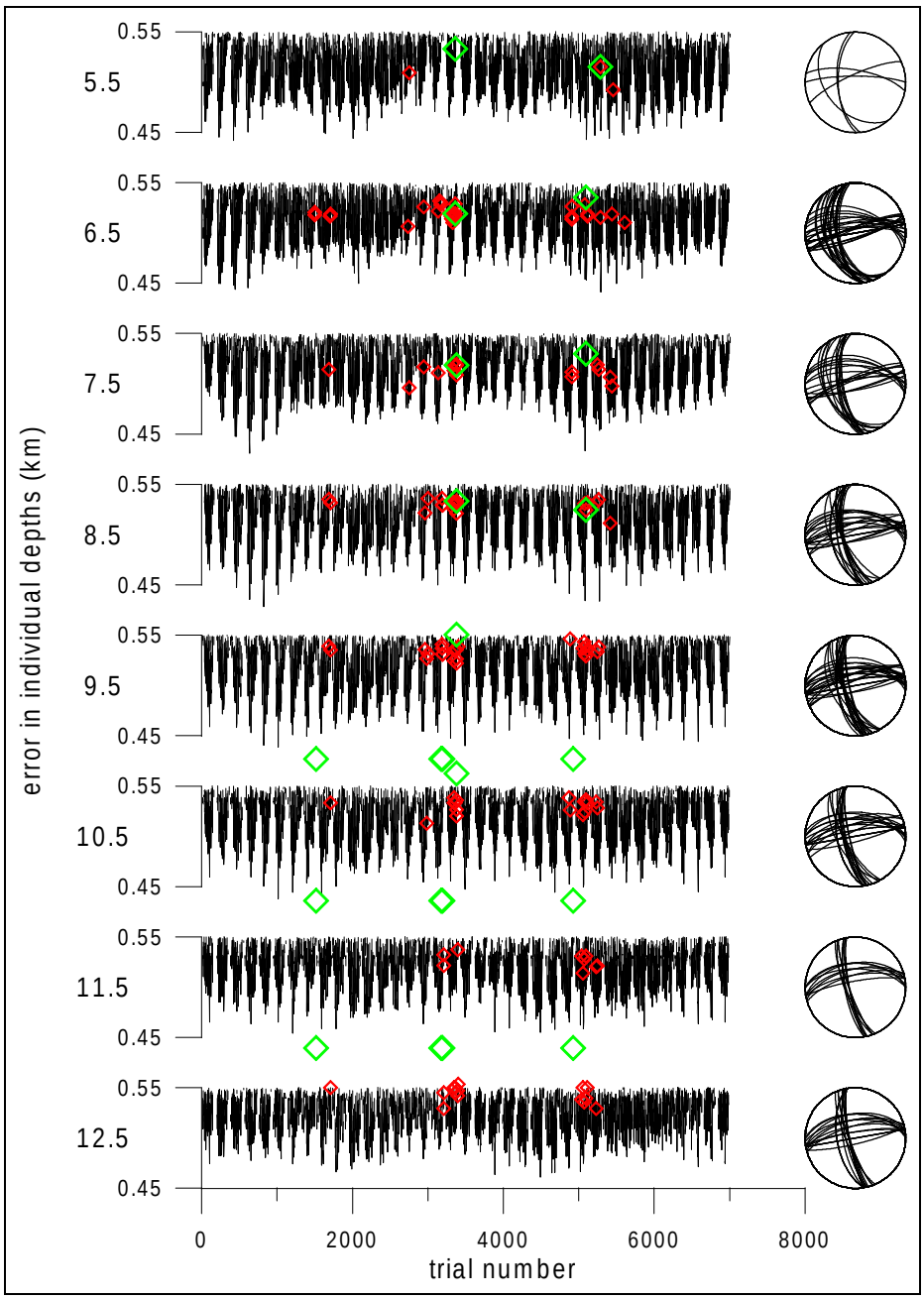

Figure B.10: Depth plot of E (black), poor-polarity P (red) and rich-polarity P (green), along with poor-polarity beach balls (2761700 Y/9).

Chapter C

Aftershock 2780500

C.0.3 Computation A/9

For error functions and depth plots, see Figs. C.2, C.3. No consistent solution can be found.

C.0.4 Computation X/9

For error functions and depth plots, see Figs. C.5, C.4. No consistent solution can be found.

Id	Code	Lat N (deg)	Lon E (deg)	Azimuth (deg)	Distance (km)
7	RAF	38.018	23.995	111.16	22.71
11	MEL	38.061	23.848	112.50	8.99
12	THR	38.139	23.761	7.61	5.27
13	MEN	38.094	23.724	274.96	2.55
16	PAR	38.153	23.737	348.33	6.92
17	KRY	38.141	23.828	50.28	8.52
20	BAR	38.135	23.791	34.80	5.82
23	AHA	38.083	23.765	133.73	1.45
25	KIF	38.096	23.799	83.71	4.04
30	PET	38.046	23.666	236.14	9.17

Table C.1: Stations engaged in the inversion (2780500 AX).

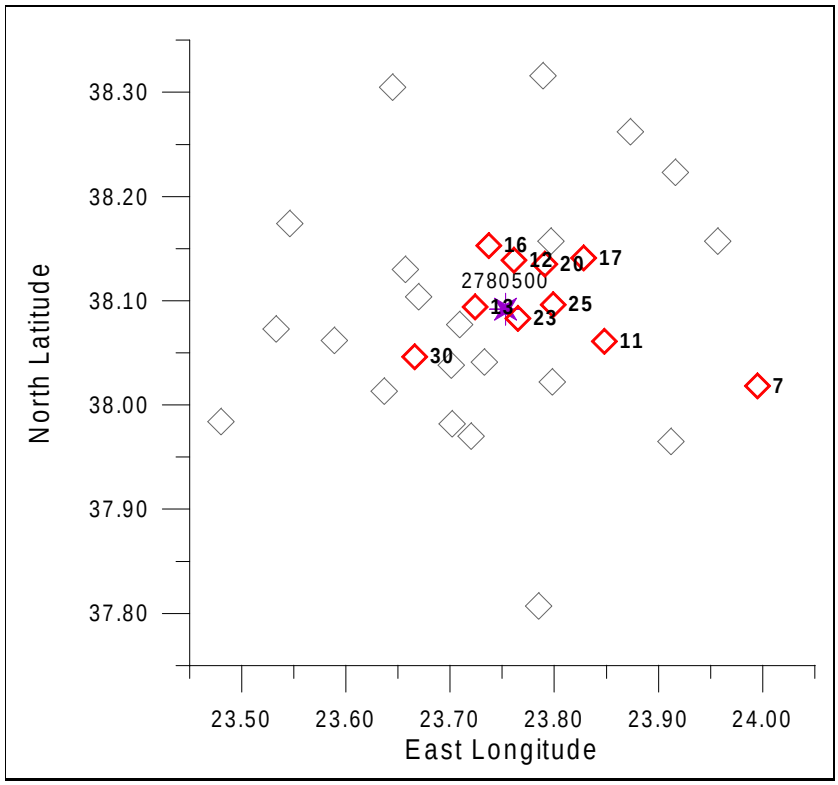

Figure C.1: Aftershock epicentre & deployment of the stations (2780500 AX).

Code	Azim (deg)	Take-off Angles (deg)								Sign
MEL	112	118	115	122	127	132	135	138	141	D
THR	7	133	134	140	144	148	150	153	155	U
MEN	274	153	155	158	161	163	165	166	167	D
PAR	348	125	124	131	136	140	143	146	148	D
KRY	50	119	117	124	129	133	137	140	143	U
BAR	34	130	131	136	141	145	148	150	153	U
AHA	133	164	165	167	169	170	171	172	172	U
KIF	83	141	142	147	151	154	157	159	160	D
PET	236	117	114	121	127	131	135	138	140	U
MAR	67	103	93	100	105	109	112	115	118	D
KAL	28	102	93	98	102	106	109	112	115	U
STE	296	103	93	99	104	108	111	114	117	D

Table C.2: Stations providing polarity data & take-off angles of the first--arrival rays (depth increasing to the right, see depth plots) (2780500 AX).

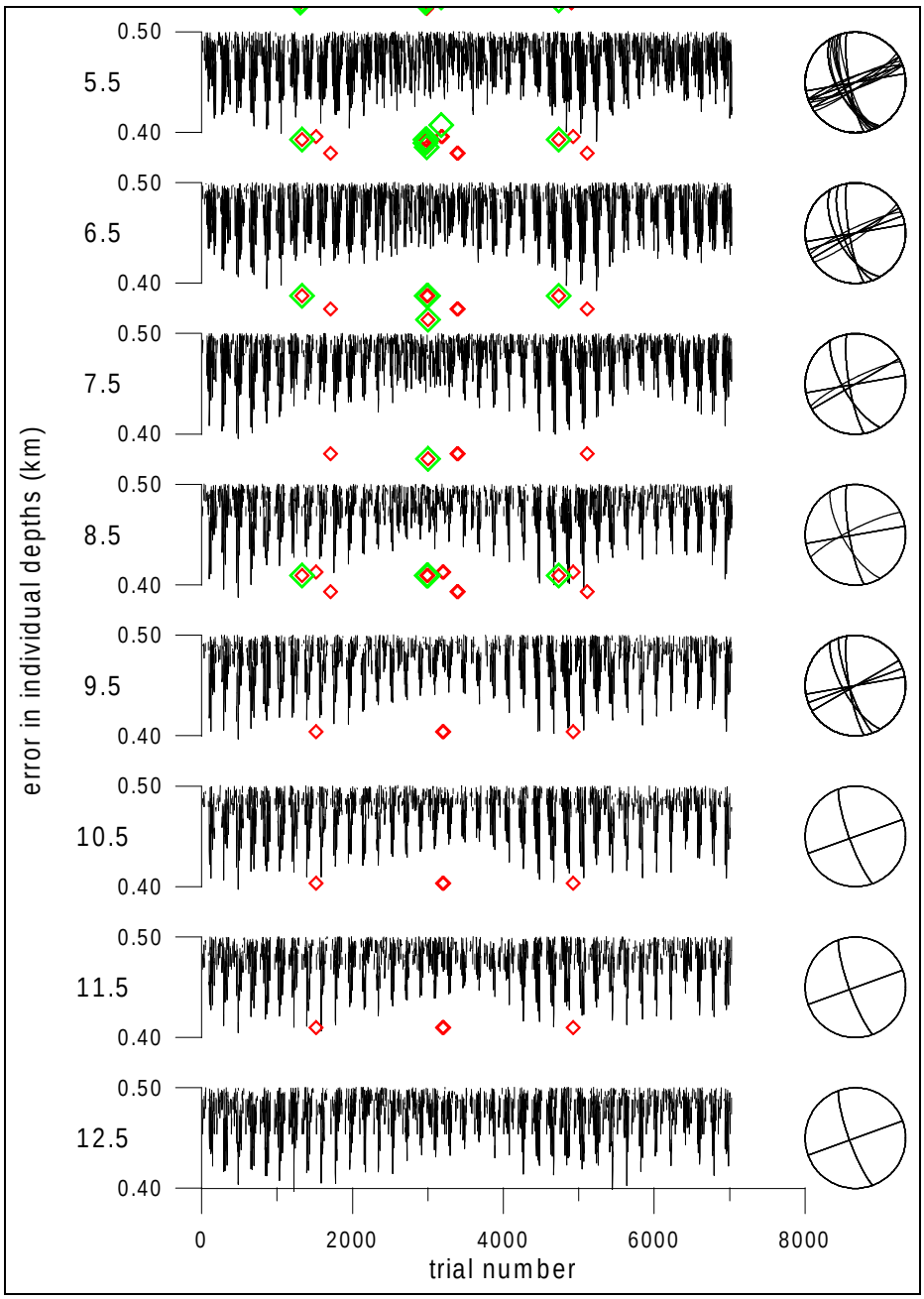

Figure C.2: Depth plot of E (black), poor-polarity P (red) and rich-polarity P (green), along with poor-polarity beach balls (2780500 A/9).

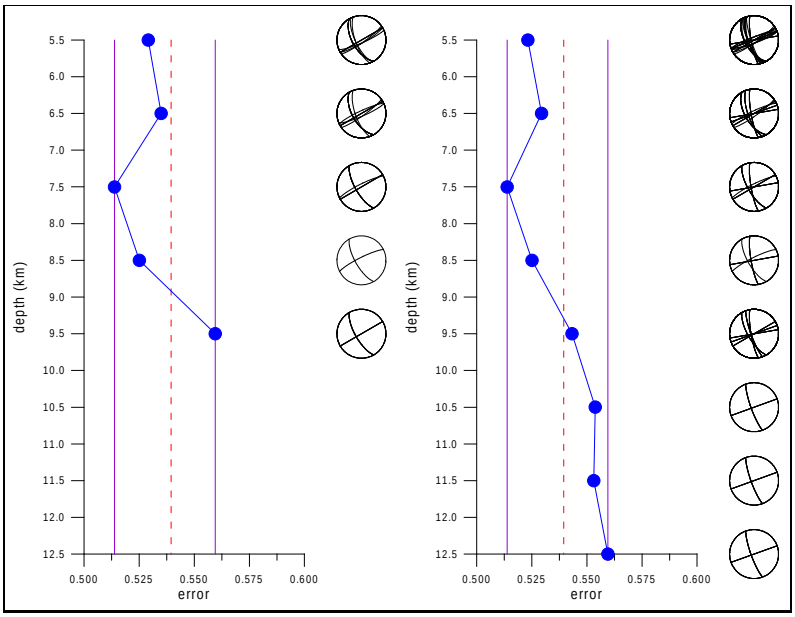

Figure C.3: Depth plot of $P(\phi_P, \delta_P, \lambda_P)$ & beach balls (2780500 A/12, A/9).

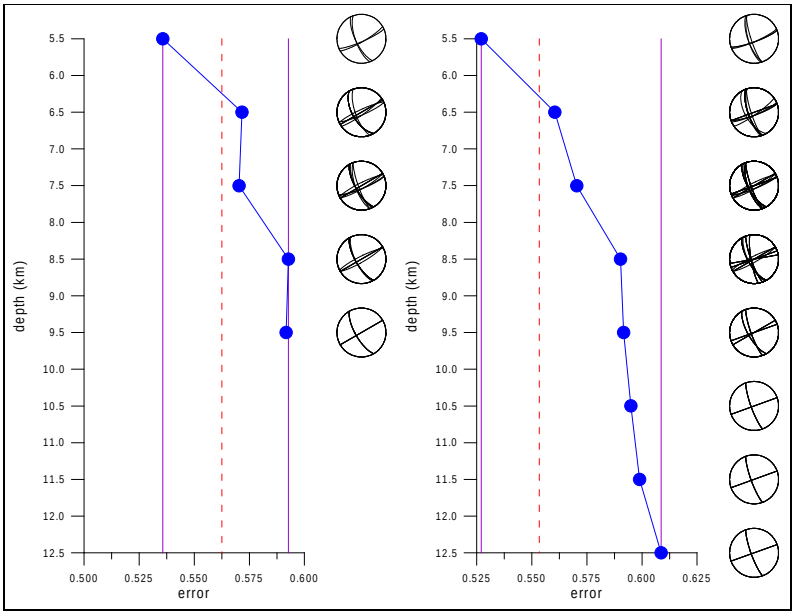

Figure C.4: Depth plot of $P(\phi_P, \delta_P, \lambda_P)$ & beach balls (2780500 X/12, X/9).

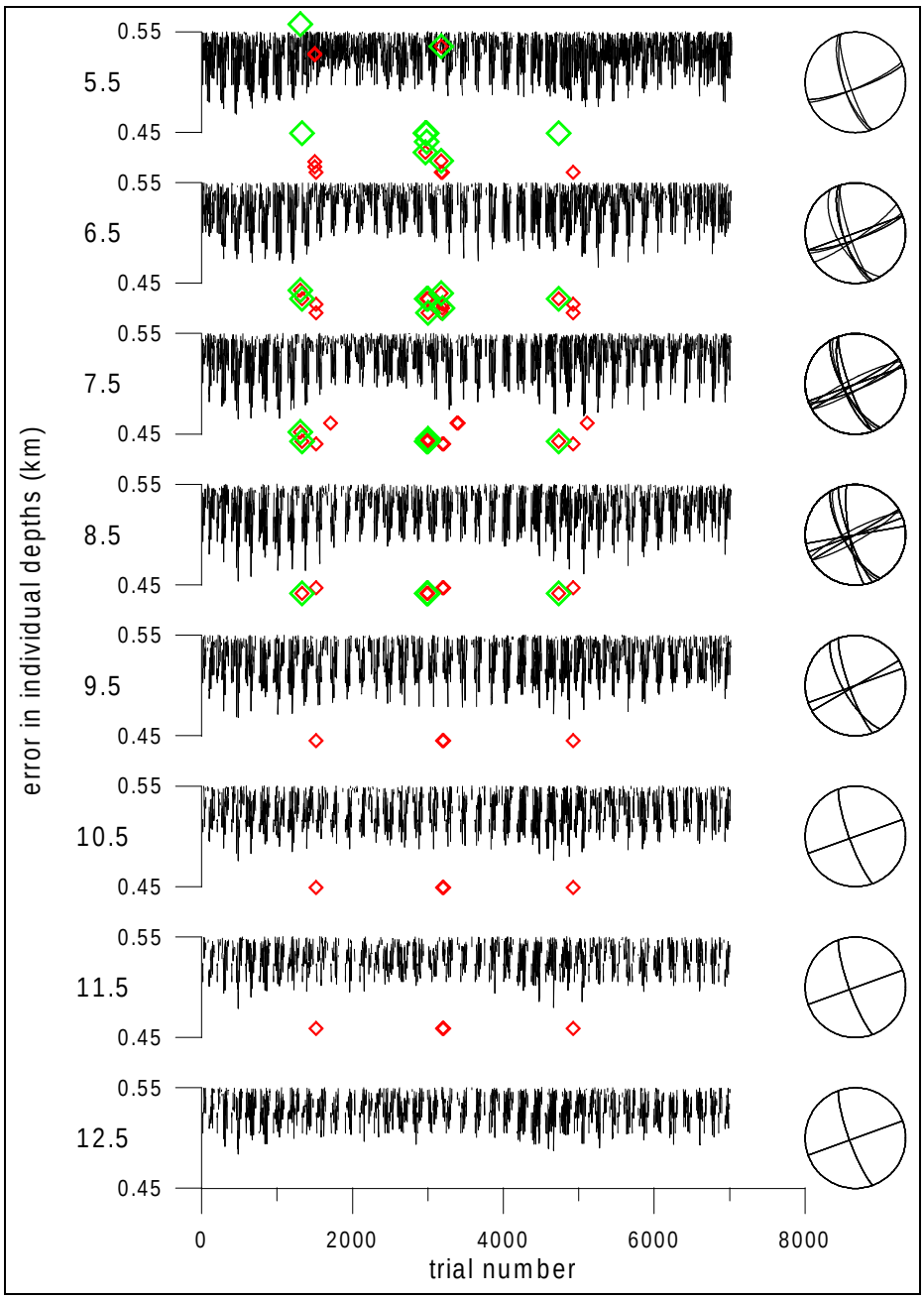

Figure C.5: Depth plot of E (black), poor-polarity P (red) and rich-polarity P (green), along with poor-polarity beach balls (2780500 X/9).

Chapter D

Aftershock 2601730

D.1 First station set

D.1.1 Computation A/10

No consistent solution can be found, see Figs. D.2, D.3.

D.1.2 Computation X/10

No consistent solution can be found, see Figs. D.5, D.4.

D.2 Second station set

D.2.1 Computation B/9

No consistent solution can be found, see Figs. D.7, D.8.

D.2.2 Computation Y/9

No consistent solution can be found, see Figs. D.10, D.9.

Id	Code	Lat N (deg)	Lon E (deg)	Azimuth (deg)	Distance (km)
1	MAG	38.073	23.533	271.58	12.34
3	ORP	38.316	23.789	20.14	29.11
7	RAF	38.018	23.995	101.53	28.67
9	KAL	38.262	23.873	39.12	27.51
12	THR	38.139	23.761	44.75	10.80
16	PAR	38.153	23.737	30.83	10.74
20	BAR	38.135	23.791	54.75	12.52
22	STE	38.174	23.546	315.95	16.08
25	KIF	38.096	23.799	75.17	11.30
27	LIO	38.077	23.709	75.77	3.16

Table D.1: Stations engaged in the inversion (2601730 AX).

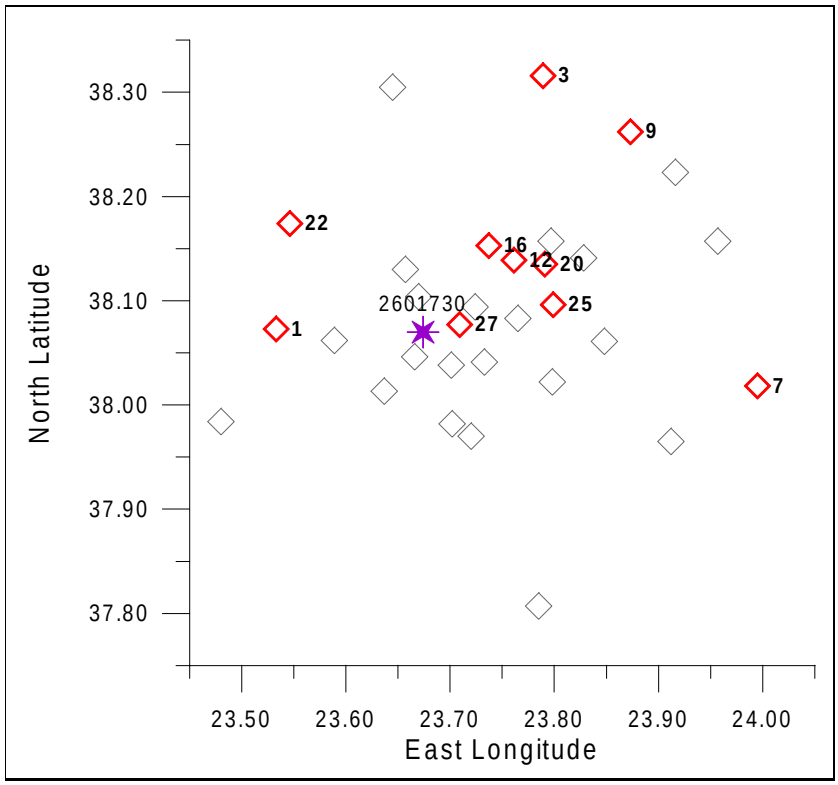

Figure D.1: Aftershock epicentre & deployment of the stations (2601730 AX).

Code	Azim (deg)	Take-off Angles (deg)								Sign
MAG	271	108	115	119	123	127	130	133	135	D
ORP	20	93	96	99	102	104	107	109	111	U
RAF	101	93	96	99	102	105	107	109	111	U
KAL	39	93	97	100	103	105	108	110	112	U
THR	44	113	119	124	128	131	134	137	139	U
PAR	30	113	119	124	128	131	134	137	139	U
BAR	54	108	114	119	123	126	130	132	135	U
STE	315	101	107	112	115	119	122	125	127	D
KIF	75	111	117	122	126	130	133	136	138	U
LIO	75	152	155	158	160	162	164	165	166	D
MAR	68	93	97	100	103	106	109	111	113	U
SPT	119	94	99	102	106	108	111	114	116	D
VUL	161	93	96	98	101	103	106	108	110	U
VAR	51	93	97	100	103	106	108	111	113	U
HAI	207	127	132	137	141	144	146	149	151	D
MEL	93	102	108	113	117	120	124	126	129	U
MEN	58	138	143	147	150	152	155	156	158	D
KRY	59	101	108	112	116	120	123	126	128	U
ASP	263	125	131	135	139	142	145	147	149	D
AHA	79	122	128	133	137	140	143	145	147	U
HAL	116	109	115	120	124	128	131	133	136	D
FLD	121	132	137	142	145	148	150	153	154	D
NLI	146	143	148	151	154	156	158	160	161	D
PET	194	155	158	161	163	164	166	167	168	D

Table D.2: Stations providing polarity data & take-off angles of the first--arrival rays (depth increasing to the right, see depth plots) (2601730 AX).

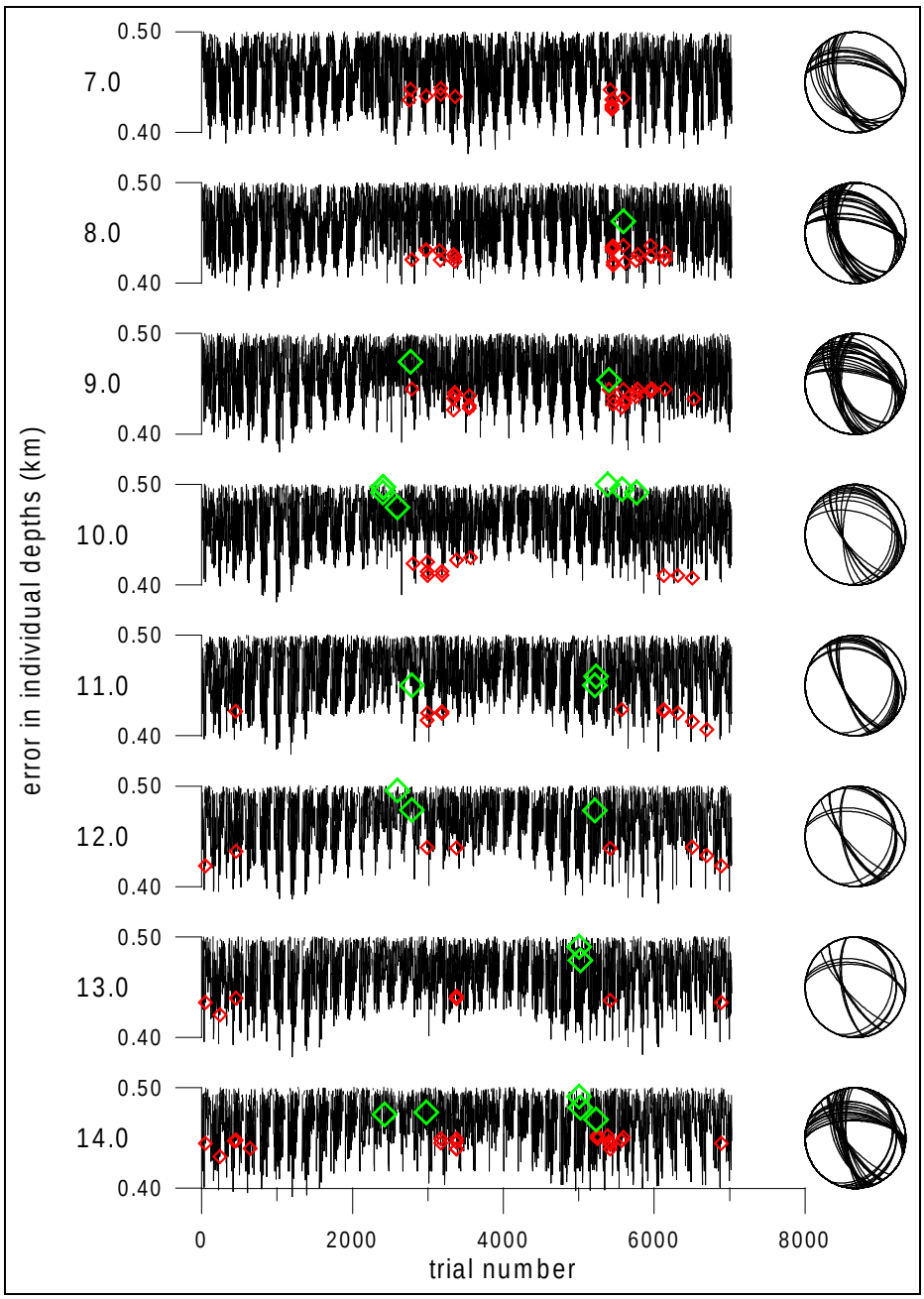

Figure D.2: Depth plot of E (black), poor-polarity P (red) and rich-polarity P (green), along with poor-polarity beach balls (2601730 A/10).

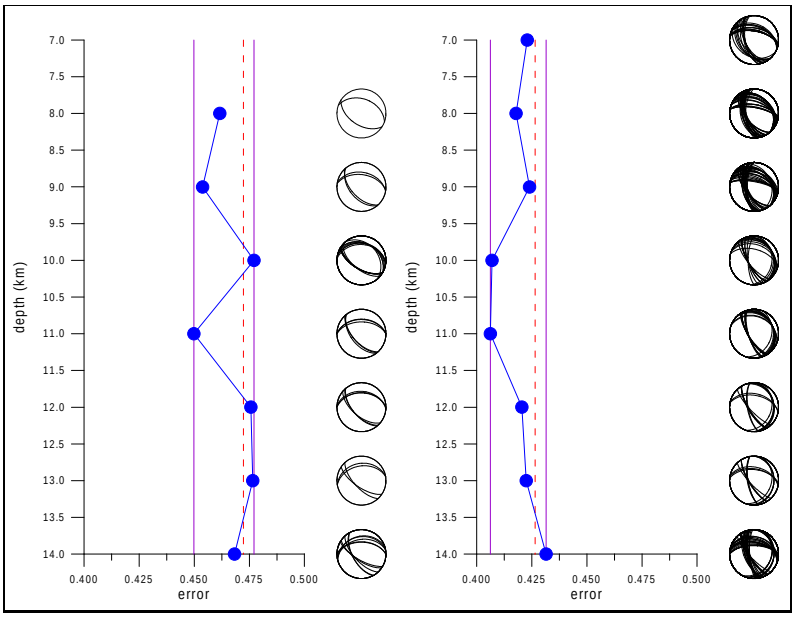

Figure D.3: Depth plot of $P(\phi_P, \delta_P, \lambda_P)$ & beach balls (2601730 A/24, A/10).

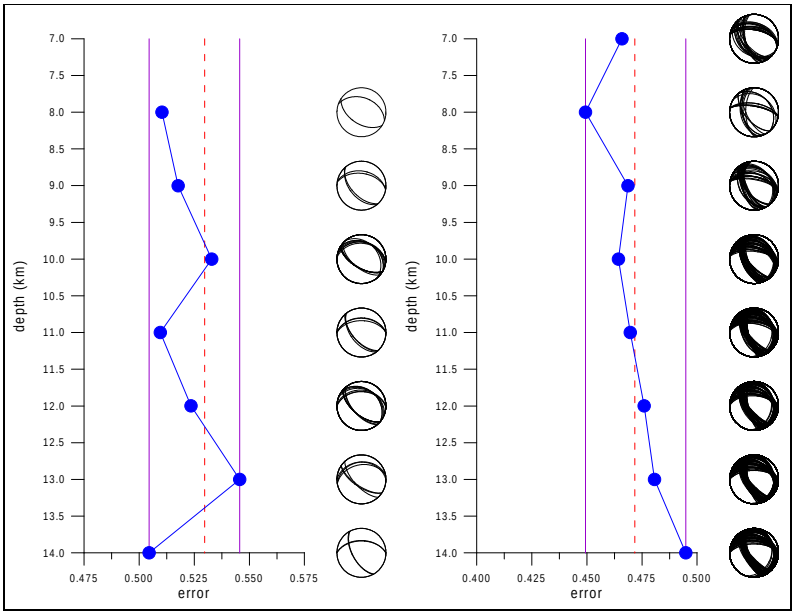

Figure D.4: Depth plot of $P(\phi_P, \delta_P, \lambda_P)$ & beach balls (2601730 X/24, X/10).

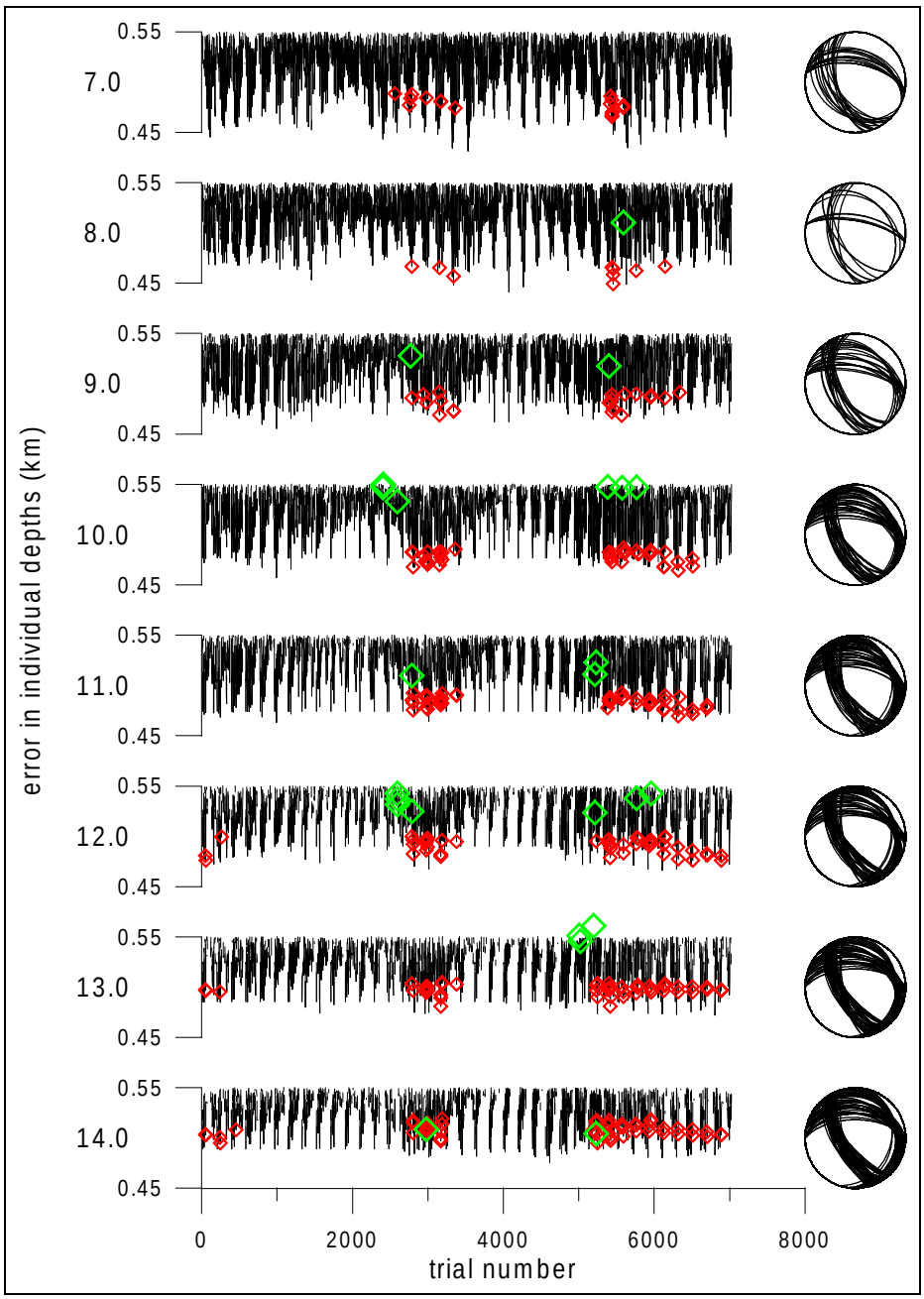

Figure D.5: Depth plot of E (black), poor-polarity P (red) and rich-polarity P (green), along with poor-polarity beach balls (2601730 X/10).

Id	Code	Lat N (deg)	Lon E (deg)	Azimuth (deg)	Distance (km)
2	INF	38.305	23.645	354.46	26.23
4	MAR	38.157	23.957	68.57	26.56
8	VAR	38.223	23.916	51.13	27.13
11	MEL	38.061	23.848	93.71	15.25
13	MEN	38.094	23.724	58.62	5.12
17	KRY	38.141	23.828	59.59	15.60
21	ASP	38.062	23.589	263.19	7.49
23	AHA	38.083	23.765	79.70	8.09
26	FLD	38.041	23.733	121.98	6.08
30	PET	38.046	23.666	194.73	2.76

Table D.3: Stations engaged in the inversion (2601730 BY).

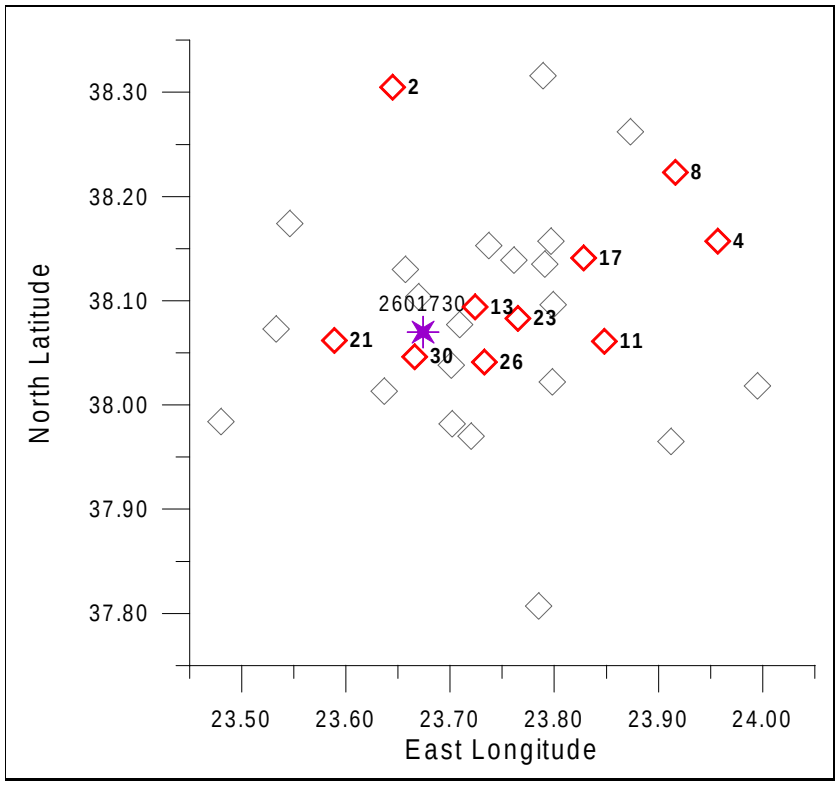

Figure D.6: Aftershock epicentre & deployment of the stations (2601730 BY).

Code	Azim (deg)	Take-off Angles (deg)								Sign
MAR	68	93	97	100	103	106	109	111	113	U
VAR	51	93	97	100	103	106	108	111	113	U
MEL	93	102	108	113	117	120	124	126	129	U
MEN	58	138	143	147	150	152	155	156	158	D
KRY	59	101	108	112	116	120	123	126	128	U
ASP	263	125	131	135	139	142	145	147	149	D
AHA	79	122	128	133	137	140	143	145	147	U
FLD	121	132	137	142	145	148	150	153	154	D
PET	194	155	158	161	163	164	166	167	168	D
MAG	271	108	115	119	123	127	130	133	135	D
ORP	20	93	96	99	102	104	107	109	111	U
SPT	119	94	99	102	106	108	111	114	116	D
VUL	161	93	96	98	101	103	106	108	110	U
RAF	101	93	96	99	102	105	107	109	111	U
KAL	39	93	97	100	103	105	108	110	112	U
HAI	207	127	132	137	141	144	146	149	151	D
THR	44	113	119	124	128	131	134	137	139	U
PAR	30	113	119	124	128	131	134	137	139	U
BAR	54	108	114	119	123	126	130	132	135	U
STE	315	101	107	112	115	119	122	125	127	D
HAL	116	109	115	120	124	128	131	133	136	D
KIF	75	111	117	122	126	130	133	136	138	U
LIO	75	152	155	158	160	162	164	165	166	D
NLI	146	143	148	151	154	156	158	160	161	D

Table D.4: Stations providing polarity data & take-off angles of the first--arrival rays (depth increasing to the right, see depth plots) (2601730 BY).

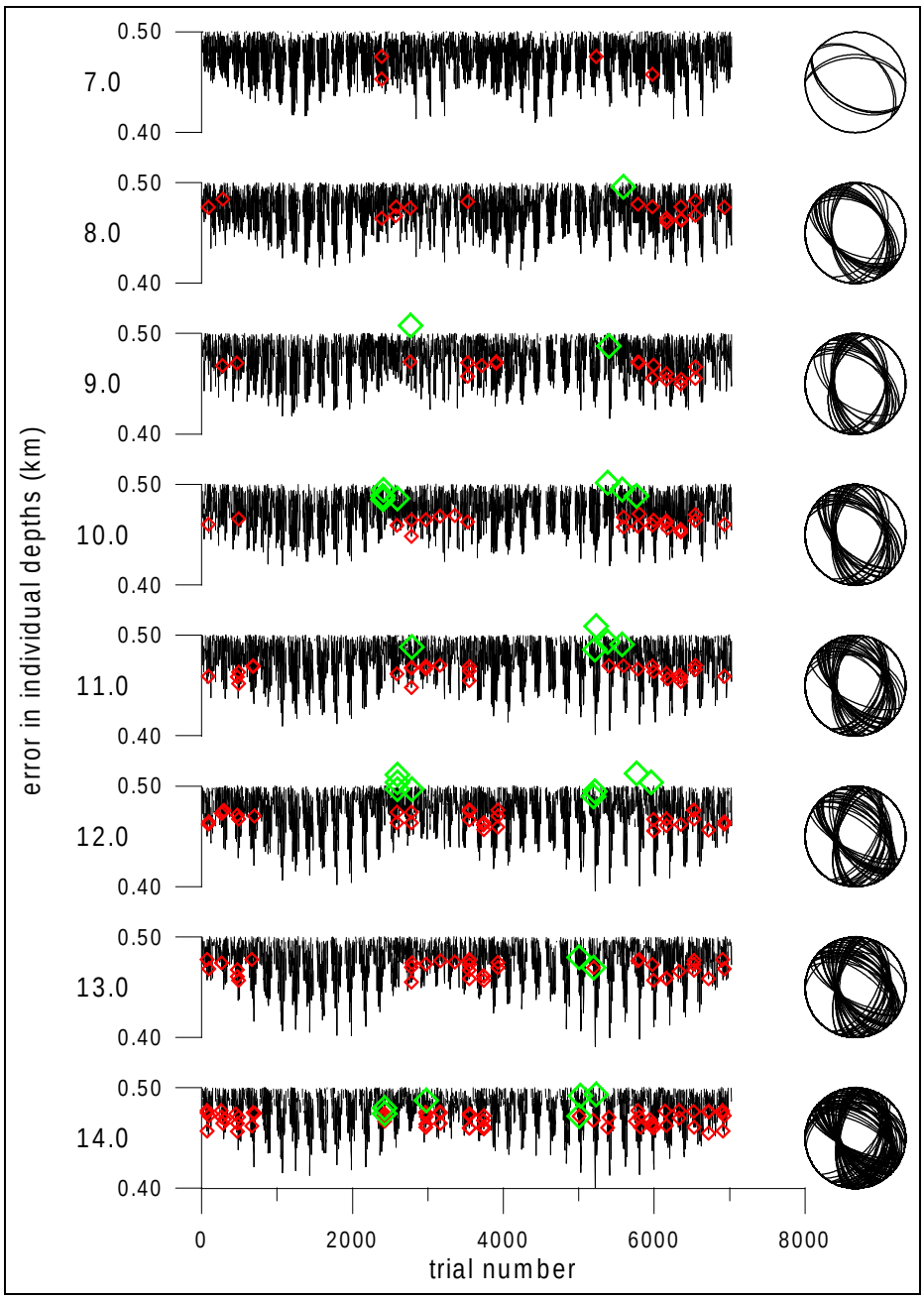

Figure D.7: Depth plot of E (black), poor-polarity P (red) and rich-polarity P (green), along with poor-polarity beach balls (2601730 B/9).

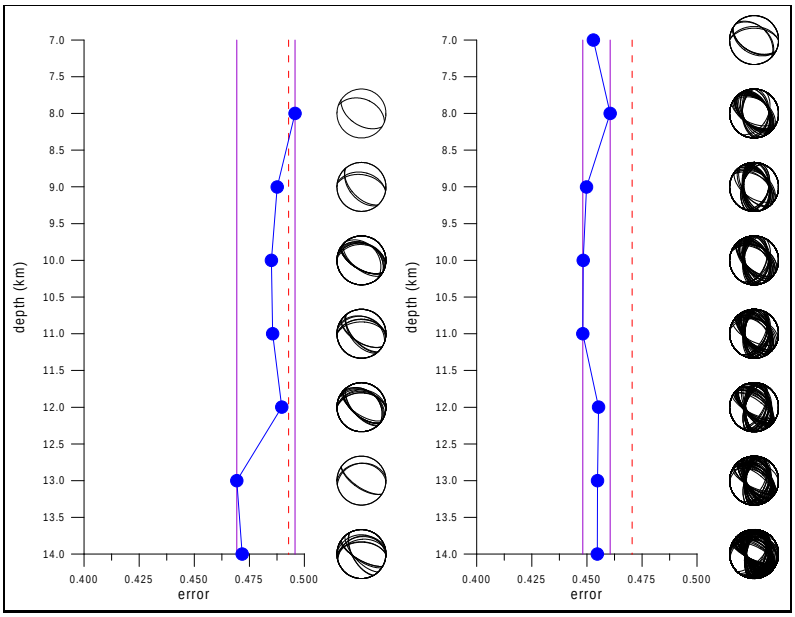

Figure D.8: Depth plot of $P(\phi_P, \delta_P, \lambda_P)$ & beach balls (2601730 B/24, B/9).

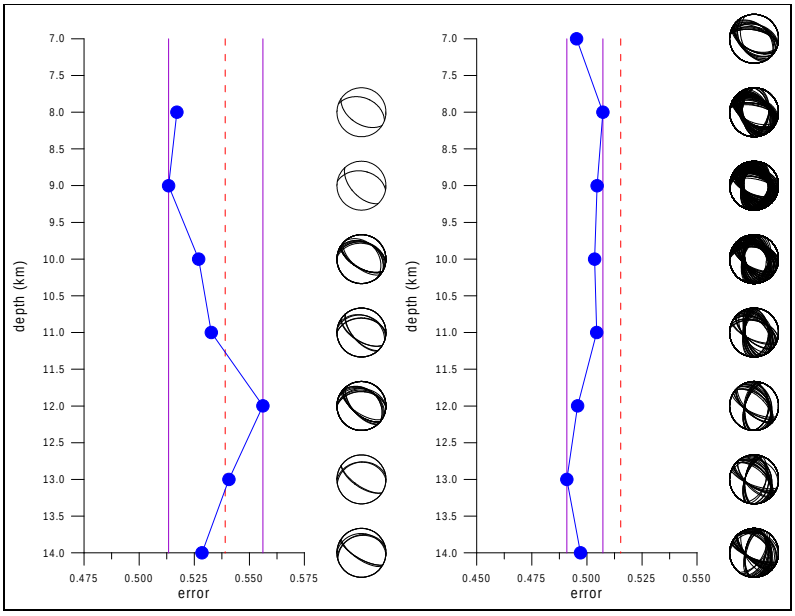

Figure D.9: Depth plot of $P(\phi_P, \delta_P, \lambda_P)$ & beach balls (2601730 Y/24, Y/9).

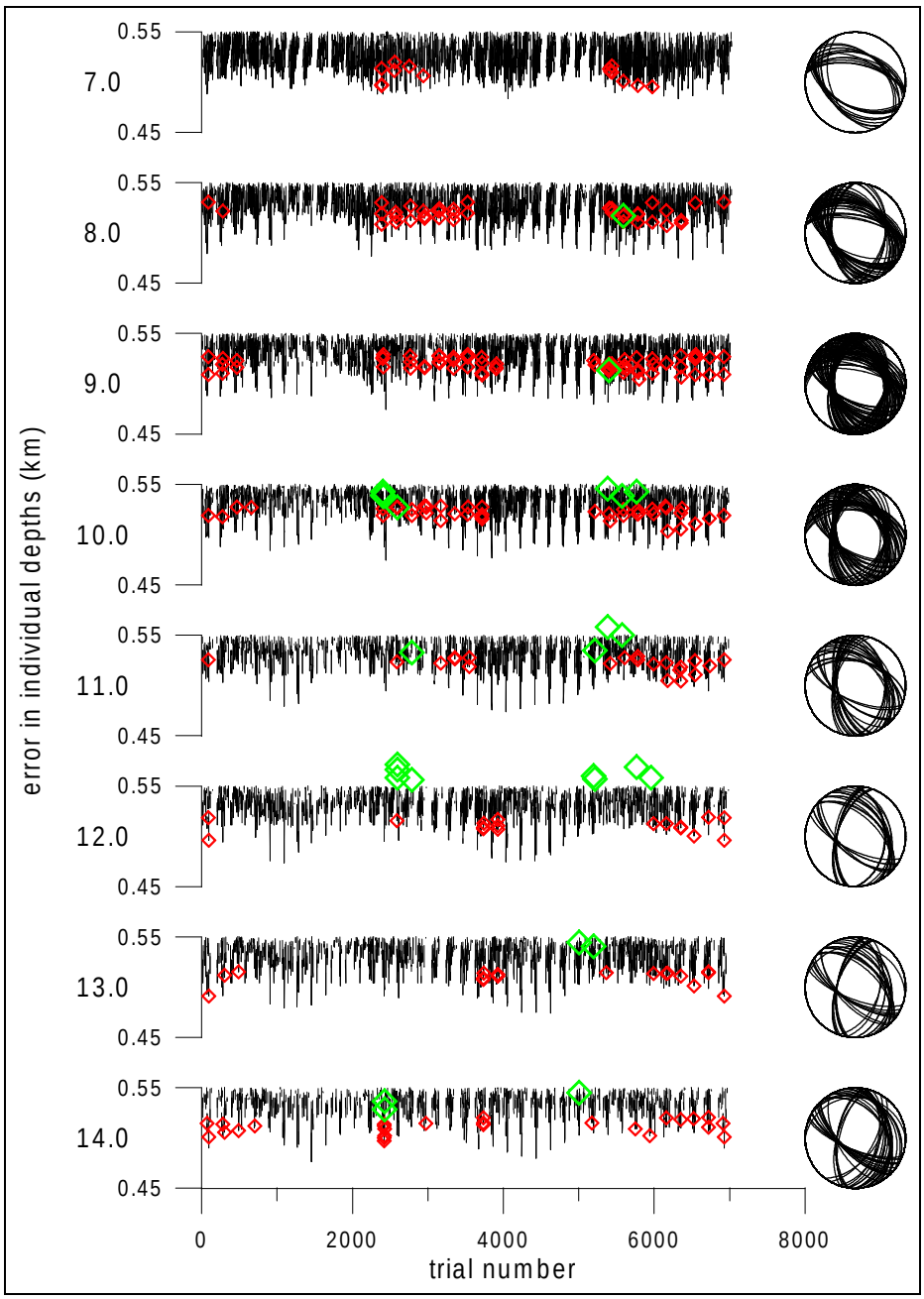

Figure D.10: Depth plot of E (black), poor-polarity P (red) and rich-polarity P (green), along with poor-polarity beach balls (2601730 Y/9).

Chapter E

Extra Inversion of Aftershock 2761700

Before discussing the new results, we report an extra inversion engaging only two most distant stations (Tab. E.1, Fig. E.1). The aftershock was chosen arbitrarily. Two poor-polarity check-point subsets are considered. The first one contains 9 check-points as in chapter B, the second one uses only 6 of these. Mind the division lines in Tab. E.2.

E.0.3 Computation A/9

According to Figs. E.2, E.3, solution at 7.5 km depth (Fig. E.6) meets the consistency criteria. Solution at 6.5 km depth (Fig. E.7) is also interesting.

E.0.4 Computation A/6

Expectably, more solutions are suggested (E.5, E.4).

E.0.5 Computation X/9

Figs. E.8, E.9 confirm the solution at 7.5 km depth, solution at 8.5 km depth is provided in addition (Figs. E.12, E.13).

E.0.6 Computation X/6

The results are not surprising (E.11, E.10).

Id	Code	Lat N (deg)	Lon E (deg)	Azimuth (deg)	Distance (km)
5	SPT	37.965	23.912	137.35	19.78
22	STE	38.174	23.546	295.02	20.53

Table E.1: Stations engaged in the inversion (Extra AX).

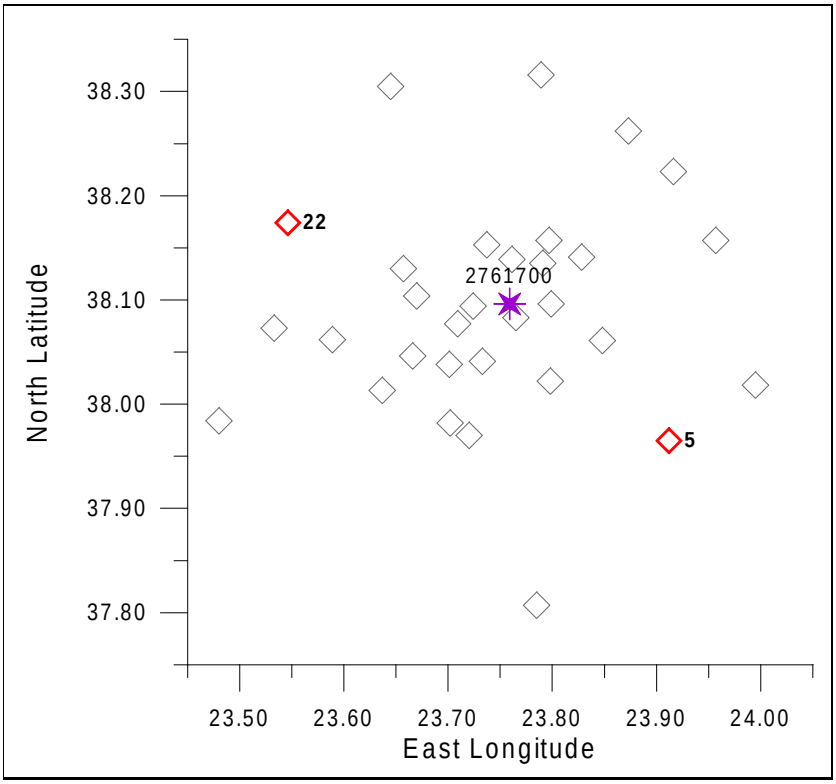

Figure E.1: Aftershock epicentre & deployment of the stations (Extra AX).

Code	Azim (deg)	Take-off Angles (deg)								Sign
SPT	137	103	93	99	104	108	112	115	117	D
MEL	116	119	116	123	128	133	136	139	142	D
MEN	265	148	150	154	157	160	162	163	165	D
MKL	292	116	112	120	125	129	133	136	139	D
BAR	32	133	135	140	145	148	151	153	155	U
STE	295	102	93	99	103	107	111	114	116	D
AHA	160	163	164	166	168	169	170	171	172	U
FLD	200	127	127	133	138	141	145	147	150	U
LIO	244	135	137	142	146	150	152	155	157	U
ORP	6	100	92	96	100	103	106	109	112	U
MAR	68	104	94	101	106	110	113	116	119	U
VUL	175	98	91	94	96	99	101	104	106	U
RAF	112	101	92	97	102	105	109	111	114	D
VAR	44	103	93	100	104	108	112	115	118	U
KAL	28	102	93	98	103	107	110	113	116	U
HAI	229	108	99	108	113	117	121	124	127	U
THR	2	136	137	143	147	150	153	155	157	D
PAR	343	126	126	132	137	141	144	147	150	D
KRY	50	121	120	127	132	136	139	142	145	U
HAL	157	118	115	122	128	132	135	139	141	U
KIF	90	145	147	151	155	157	159	161	163	U
GEO	201	109	100	109	114	118	122	125	128	U

Table E.2: Stations providing polarity data & take-off angles of the first--arrival rays (depth increasing to the right, see depth plots) (Extra AX).

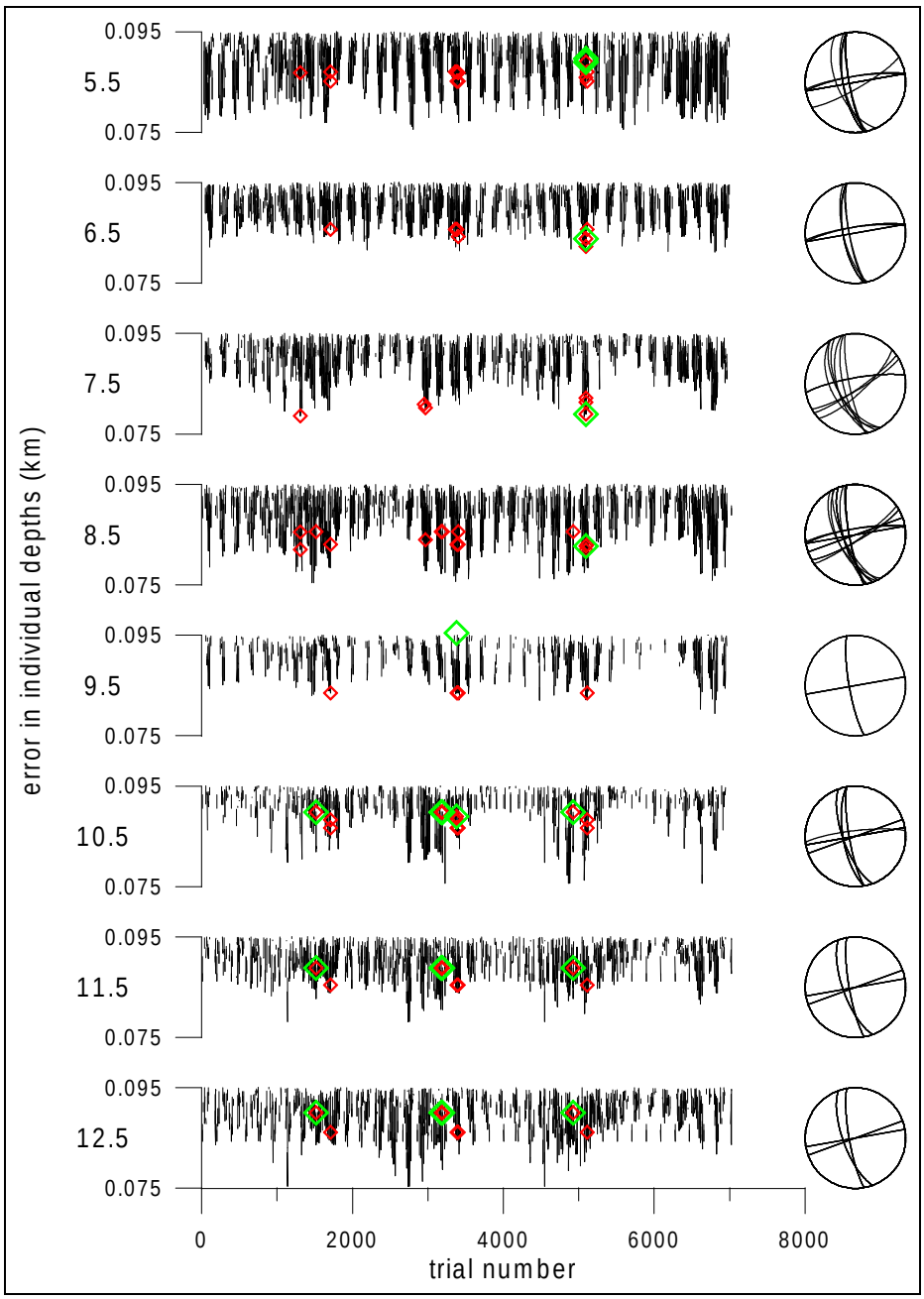

Figure E.2: Depth plot of E (black), poor-polarity P (red) and rich-polarity P (green), along with poor-polarity beach balls (Extra A/9).

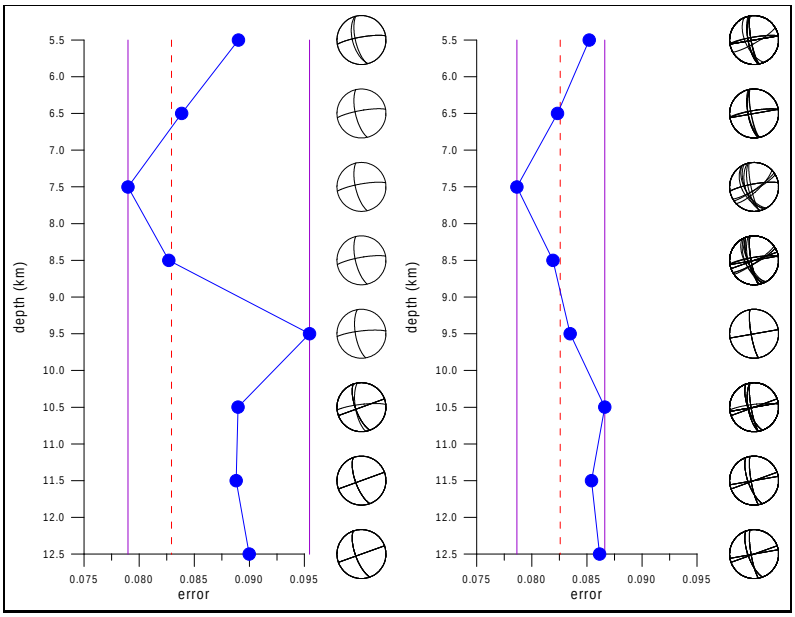

Figure E.3: Depth plot of $P(\phi_P, \delta_P, \lambda_P)$ & beach balls (Extra A/22, A/9).

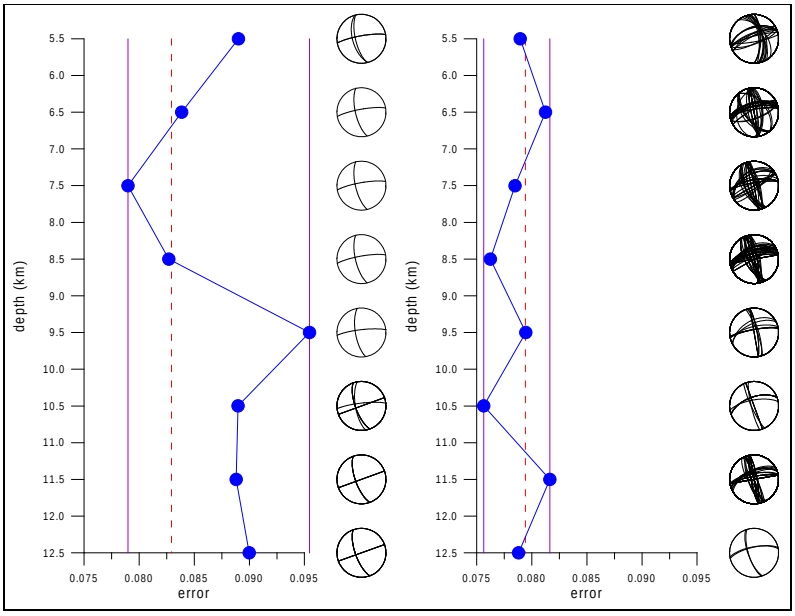

Figure E.4: Depth plot of $P(\phi_P, \delta_P, \lambda_P)$ & beach balls (Extra A/22, A/6).

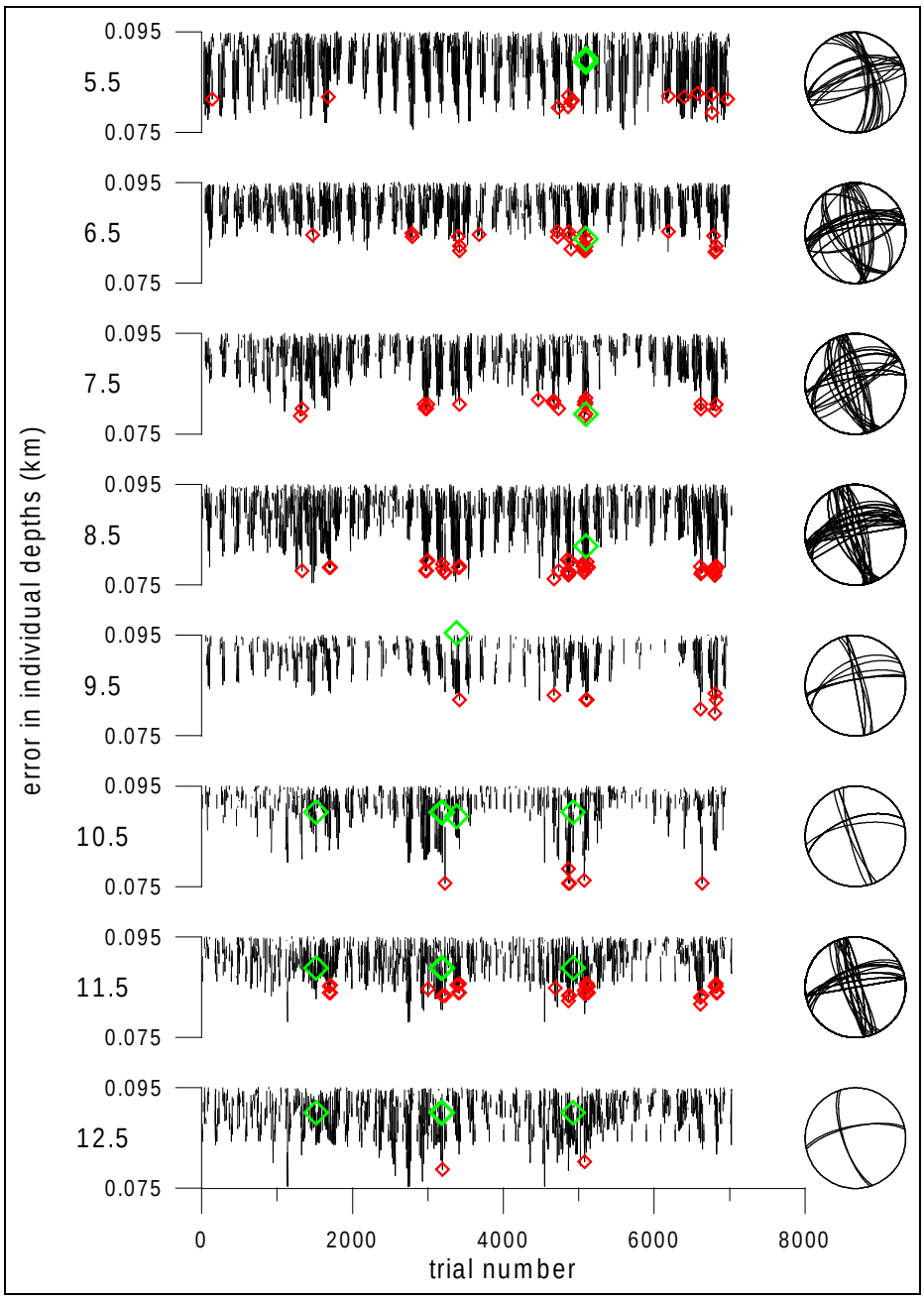

Figure E.5: Depth plot of E (black), poor-polarity P (red) and rich-polarity P (green), along with poor-polarity beach balls (Extra A/6).

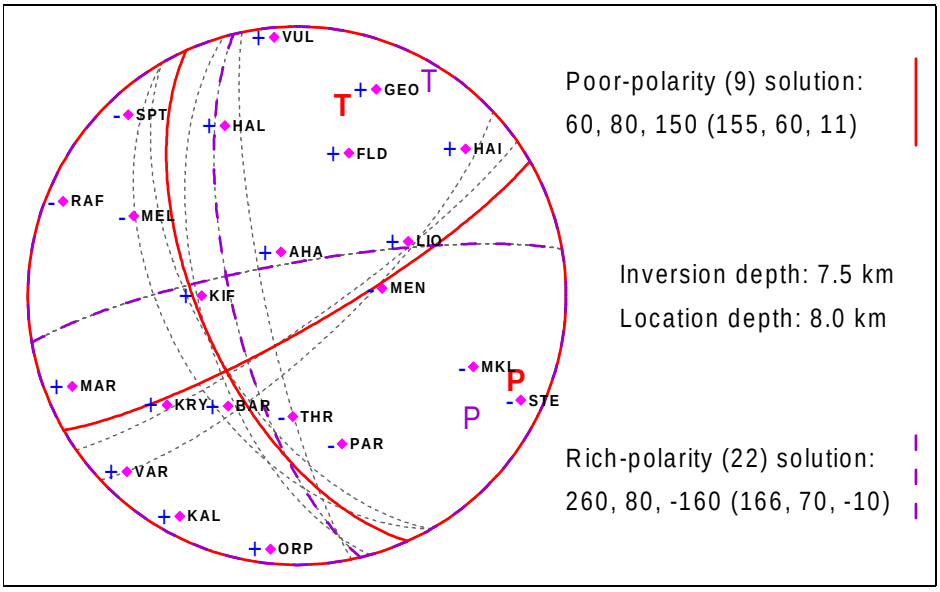

Figure E.6: Nodal lines of solution at 7.5 km depth (extra 2761700 A/9).

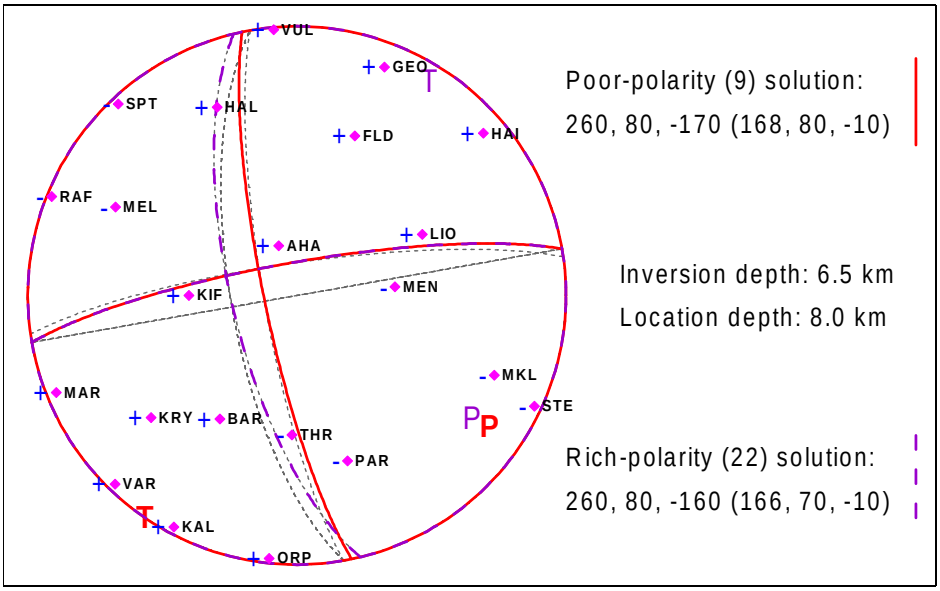

Figure E.7: Nodal lines of solution at 6.5 km depth (Extra A/9).

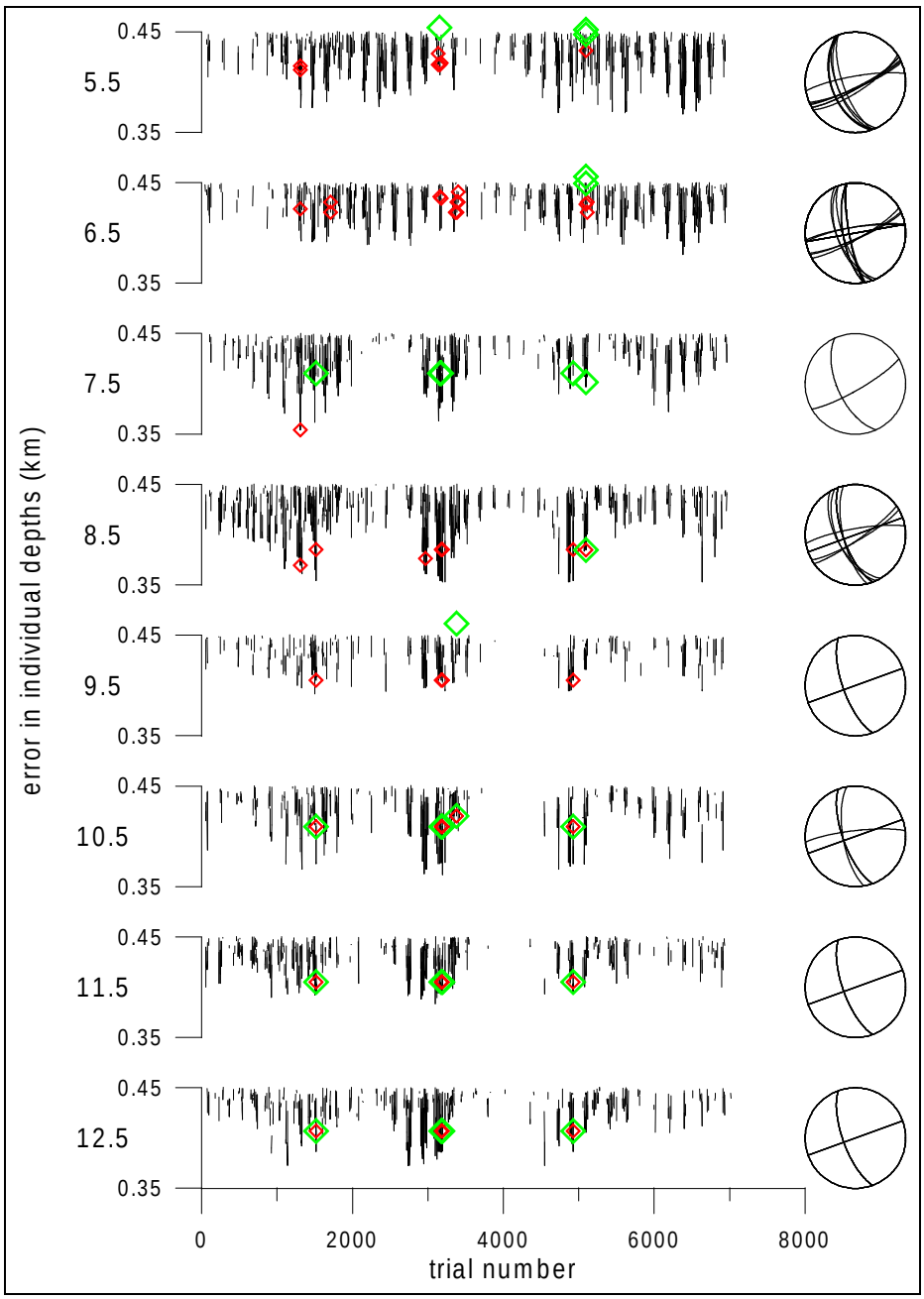

Figure E.8: Depth plot of E (black), poor-polarity P (red) and rich-polarity P (green), along with poor-polarity beach balls (Extra X/9).

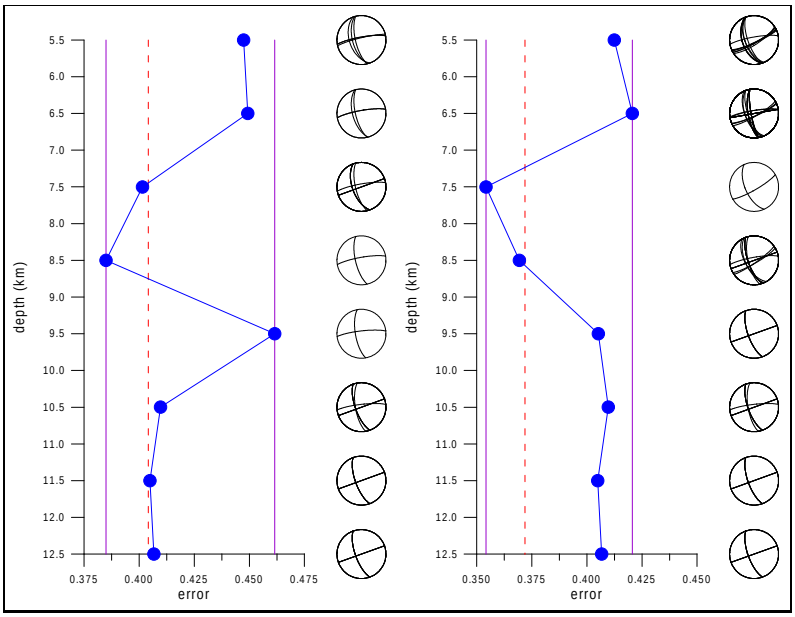

Figure E.9: Depth plot of $P(\phi_P, \delta_P, \lambda_P)$ & beach balls (Extra X/22, X/9).

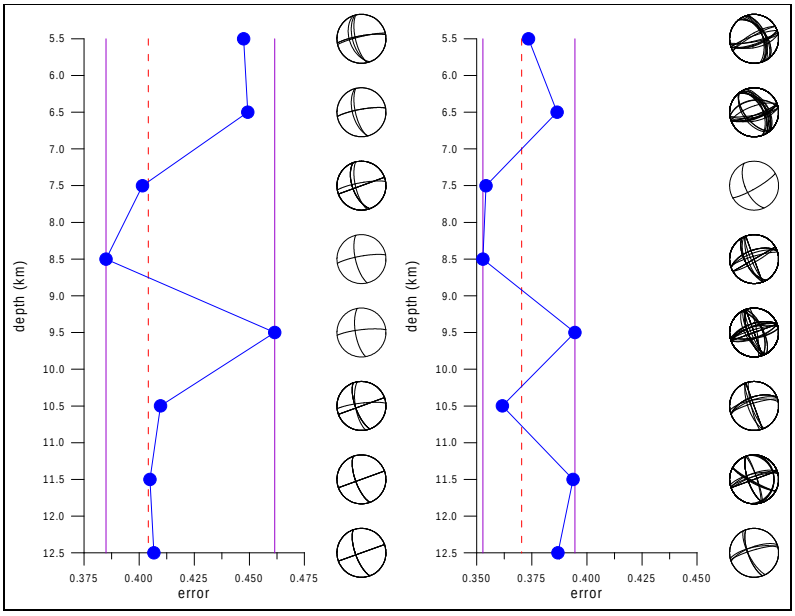

Figure E.10: Depth plot of $P(\phi_P, \delta_P, \lambda_P)$ & beach balls (Extra X/22, X/6).

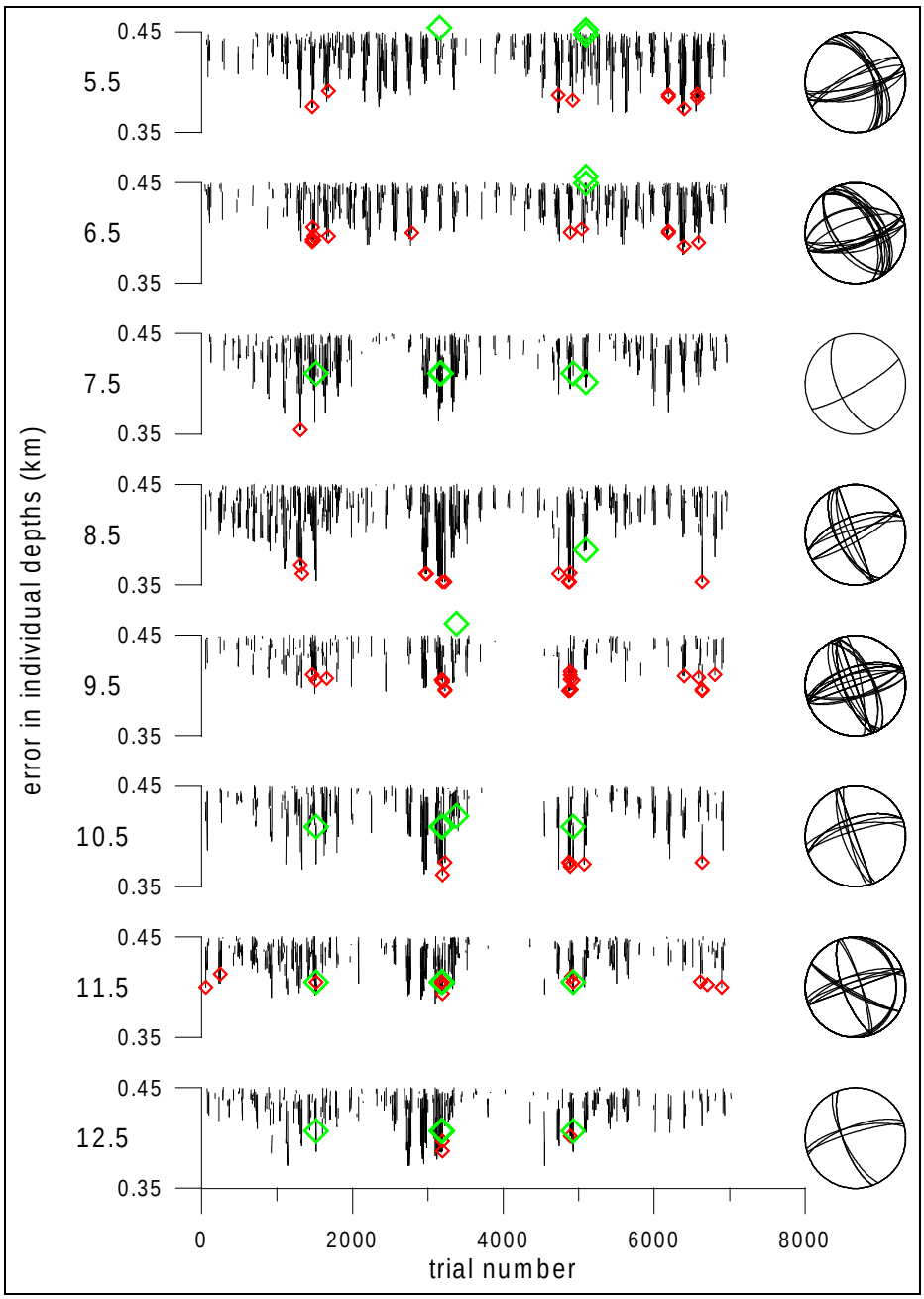

Figure E.11: Depth plot of E (black), poor-polarity P (red) and rich-polarity P (green), along with poor-polarity beach balls (Extra X/6).

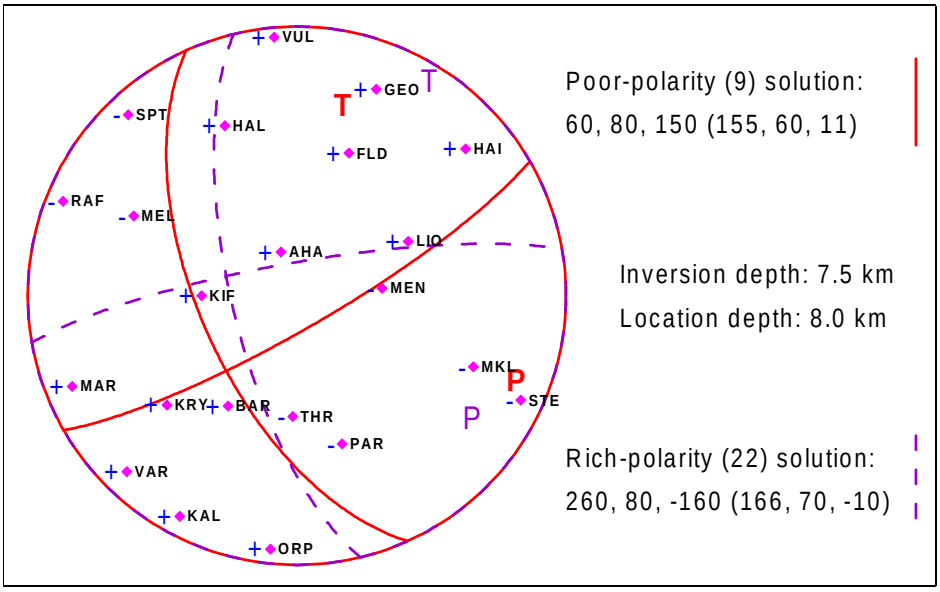

Figure E.12: Nodal lines of solution at 7.5 km depth (Extra X/9).

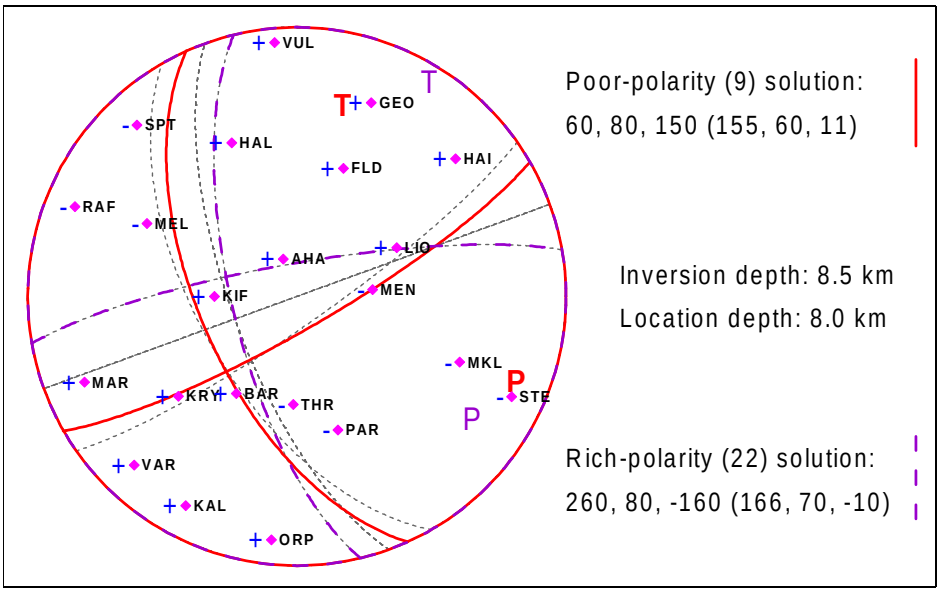

Figure E.13: Nodal lines of solution at 8.5 km depth (Extra X/9).

Conclusion

As discussed in the original work, success of the ASPO method depends on the number of stations engaged in the inversion. The re-computed results are critical, however the extra inversion solves the problem well.

Note that nearness of stations harms the accuracy of determination of azimuth, which is used not only in rotation of the spectra, but even in projection of the check-points onto the focal sphere. On the other hand, distant stations may provide low frequencies rather than those required by the inversion frequency domain.

We have seen that the formal approach to the method fails in general. The input data should be handled individually in order to verify all physical assumptions. Then, the method is applicable.